

# A Nonlinear Iterative Reconstruction and Analysis Approach to Shape-Based Approximate Electromagnetic Tomography

Naren Naik, Jerry Eriksson, Pieter de Groen, and Hichem Sahli

**Abstract**—A nonlinear Helmholtz-equation-modeled electromagnetic tomographic reconstruction problem is solved for the object boundary and inhomogeneity parameters in a damped Tikhonov-regularized Gauss–Newton (DTRGN) solution framework. In this paper, the object is represented in a suitable global basis, whereas the boundary is expressed as the zero level set of a signed-distance function. For an explicit parameterized boundary-representation-based reconstruction scheme, analytical Jacobian and Hessian calculations are made to express the changes in scattered field values w.r.t. changes in the inhomogeneity parameters and the control points in a spline representation of the object boundary, via the use of a level-set representation of the object. Even though, in this paper, a homogeneous dielectric is considered and a spline representation has been used to represent the boundary, the formulation can be used for a general global basis representation of the inhomogeneity as well as arbitrary parameterizations of the boundary, and is generalizable to three dimensions. Reconstruction results are presented for test cases of landminelike dielectric objects embedded in the ground under noisy data conditions. To confirm convergence and, at times, to know which of the obtained iterates are closer to the actual unknown solution, using a perturbation theory framework, a local (Hessian-based) convergence analysis is applied to the DTRGN scheme for the reconstruction, yielding estimates of convergence rates in the residual and parameter spaces.

**Index Terms**—Boundary reconstruction, Gauss–Newton method, local analysis, nonlinear tomography, subsurface imaging, Tikhonov regularization.

## I. INTRODUCTION

THE NEED for nonlinear reconstruction approaches occurs in many branches of electromagnetic tomographic imaging. Some examples are wave-equation-based diffraction tomography, electrical impedance tomography, and diffusion optical tomography, to name just a few. The area of tomo-

graphic subsurface imaging is of interest in important applications such as geophysical prospecting and landmine detection, to name only a couple. Typically, the reconstruction of the desired parameters is achieved in the following possible ways: 1) by a minimization of an objective functional comprising the residual of the measured and modeled data when either the full scattering operator [1]–[3] or an approximate operator such as a first- or a second-order Born approximation [4], [5] is considered and 2) via analytical methods, which are based on approximations of the forward operator [6].

The minimization class of problems, being ill posed in nature, needs additional *a priori* information (such as support of the object) to aid the convergence of the solution scheme to the desired correct solution. The motivations of using boundary information in a tomographic reconstruction are typically to lend stability to the iterative reconstruction scheme (by better demarcation of object support constraints and also by the possible reduction of the number of parameters characterizing the object) or to solve an “approximate” inverse scattering problem wherein the object shape, location, and an approximate (as against a more exact) estimate of the object’s interior physical parameter values are reconstructed. The iterative “shape-based” approximate reconstruction schemes broadly fall into two categories. The objective functional minimized in the first class has as unknowns the coefficients in an explicit parametric representation for the boundary curve(s), whereas, in the latter class, the unknowns are the values of a set function representing the image, with the zero level set of that function representing the boundary. While the first (explicit representation) class of schemes has the advantage of fewer unknowns, which is useful in potential 3-D reconstructions, the second (implicit representation) class is better suited to handle topological changes in the evolving shape of the boundary. In this paper, we have formulated a scheme for the solution and convergence analysis of the nonlinear 2-D approximate reconstruction problem in the first class of schemes, in a framework for arbitrary parameterizations, that is conceptually generalizable to three dimensions as well. We use a level-set representation for the shapes in order to calculate the first- and second-order shape and electromagnetic parameter derivatives of the objective functional in a parameterized representation and not in the more customary implicit level-set representation of the boundaries.

Miller *et al.* [7] solved the approximate inverse scattering problem using a partially nonlinear Born iterative scheme with a spline representation of the image boundary and a global basis representation for the object and background inhomogeneities. They use a greedy-search-type technique to find the best change

Manuscript received May 30, 2006; revised September 30, 2007. This work was supported in part by the Vrije Universiteit Brussel Research Council under Concerted Action Project GOA-20 on “Numerical issues in tomographic shallow subsurface imaging.”

N. Naik is with the Department of Mechanical Engineering and the College of Engineering, University of Canterbury, Christchurch 8140, New Zealand (e-mail: naren.naik@canterbury.ac.nz; nnaikt@yahoo.com).

J. Eriksson is with the Department of Computing Science, Umeå University, 901 87 Umeå, Sweden (e-mail: jerry@cs.umu.se).

P. de Groen is with the Department of Mathematics, Vrije Universiteit Brussel, 1050 Brussels, Belgium (e-mail: pdegroen@vub.ac.be).

H. Sahli is with the Department of Electronics and Informatics (ETRO), Vrije Universiteit Brussel, 1050 Brussels, Belgium, and also with the Interuniversitair Micro-Elektronica Centrum, B-3001 Leuven, Belgium (e-mail: hsahli@etro.vub.ac.be).

Color versions of one or more of the figures in this paper are available online at <http://ieeexplore.ieee.org>.

Digital Object Identifier 10.1109/TGRS.2008.916077

of control points at a given iteration. The work of Bonnard *et al.* [8] uses a rigorous integral-equation-based formulation for homogeneous dielectrics to solve the corresponding reconstruction problem, with the shape parameters and the inhomogeneity value being the unknowns. More recently, Kilmer *et al.* [9] have derived a Gauss–Newton-type algorithm to solve the approximate inverse scattering problem for the shape parameters as well as inhomogeneity coefficients in a suitable typically “slowly varying” basis for 3-D ellipsoidal objects in optical tomography. The nomenclature of “Gauss–Newton type,” rather than “Gauss–Newton,” is used by them, because some of the Frechet derivatives w.r.t the shape parameters are evaluated through the use of finite-difference approximations, and the columns of the Jacobian are only approximately solved by an iterative method. The work of Ye *et al.* [10] gives confidence intervals for reconstructed shapes but does not reconstruct the inhomogeneity values since it deals with conducting objects. In addition, this approach uses the domain derivative approach to evaluate the Frechet derivatives, which is a far-field relation.

In the second (implicit) class of methods, Dorn *et al.* [11] used a level-set-based formulation to solve the shape reconstruction problem, assuming knowledge of the object’s electromagnetic parameters. The boundary is implicitly represented as the zero level set of a function, and that function is iteratively solved to get the boundaries. Feng *et al.* [12] presented a curve evolution approach to solving the linear approximate reconstruction for arbitrary shapes and inhomogeneities. The recent work of Chung *et al.* [13] solves the nonlinear electrical impedance tomography problem for both the shape and conductivity in a level-set framework.

We mention a number of recent contemporary works on the problem that have appeared during the course of review of this paper. Zacharopoulos *et al.* [15] simultaneously reconstructed shape and optical parameters for noiseless data in a frequency-domain 3-D elliptic inverse problem in diffuse optical tomography for piecewise constant objects using a spherical harmonics parametrization of the boundary in a boundary element method discretization scheme. For an alternating minimization scheme for shape and optical parameters, they derive the shape of Frechet derivatives with a fully adjoint-based calculation [17],<sup>1</sup> which, in turn, uses the boundary-integral expression of the seminal work of [18], relating variations of internal parameters to infinitesimal boundary variations. In a more recent work, Firoozabadi *et al.* [16] solved a 2-D shape and electrical parameter reconstruction problem for a subsurface tomography problem using a fully nonlinear scheme, where the Frechet derivative calculations for the shape parameters use analytical differentiation w.r.t boundary point coordinates using recurrence relations for Bessel function derivatives, which arise due to the specific nature of fields obtained in the semianalytic mode matching scattering model employed in this paper for the subsurface imaging problem.

In the present nonlinear scheme, to solve the approximate reconstruction problem, the object is represented in a suitable global basis, whereas the boundary is expressed as the zero

level set of a signed-distance function. Analytical Jacobian calculations are made to express the change in scattered field values w.r.t. changes in the inhomogeneity parameters and the control points in a spline representation of the object boundary, via the use of a level-set representation of the object. Even though, in this paper, a homogeneous dielectric is considered and a spline representation has been used to represent the boundary, the formulation can be used for a general global basis representation of the inhomogeneity as well as arbitrary parameterizations of the boundary, and is generalizable to three dimensions.

A damped Tikhonov-regularized Gauss–Newton (DTRGN) approach is then applied to the residual-norm objective functional to arrive at the desired reconstruction of the boundary and object parameters. Furthermore, using a perturbation theory framework as in [2] and [14], a Hessian-based local convergence analysis is applied to the DTRGN scheme for the reconstruction, yielding estimates of convergence rates in the residual and parameter spaces.

Thus, the contribution of this paper lies in 1) the analytical calculation of the needed Jacobian and Hessian matrices w.r.t both the electromagnetic and shape parameters in the explicit-curve-representation setting of this paper, in a framework for arbitrary parameterizations and for (in general) smoothly varying inhomogeneities valid for near- and far-field measurements, that is conceptually generalizable to three dimensions and 2) the application of the aforementioned second-order convergence analysis to make inferences on the obtained iterates.

Our algorithm differs from that in [15] in that, with the objective of doing a second-order Hessian-based analysis of the reconstructions, we use an explicitly defined “tubular neighborhood” of the boundary coupled with an approximate Heaviside-function-based representation of the object interior, in the Frechet derivative calculations, that yields analytical relations for the shape as well as the electromagnetic parameter derivatives. The conceptual relation between the Frechet derivatives calculated via our tubular neighborhood approach and those calculated directly using the boundary-integral relation of [18] can be seen from our derivation of the continuous-domain Frechet derivative (in Section III-A), where the limiting relation between the expressions is shown. In addition to our present work being applicable to fully numerical solvers of the forward problem, the formulation of the Frechet derivative calculations are different from that in [16]. Thus, the formulations to calculate the Jacobian are different in our work w.r.t to these works [15], [16]; furthermore, we evaluate analytical expressions for the Hessian matrix and perform a Hessian-based convergence analysis on the reconstructions obtained for noisy data.

This paper is organized as follows. Section II presents the problem formulation. Section III derives the continuous-domain Frechet derivatives and the discrete-domain Jacobian. Section IV presents the DTRGN reconstruction scheme and a local convergence analysis applied to the DTRGN reconstruction scheme, yielding estimates of convergence rates in the residual and parameter spaces. Results of reconstruction and analysis of some example minelike phantoms in a ground-penetrating radar (GPR) tomography setting are presented in Section V, whereas the conclusions are given in Section VI.

<sup>1</sup> Also released on the web during the review process of this paper.

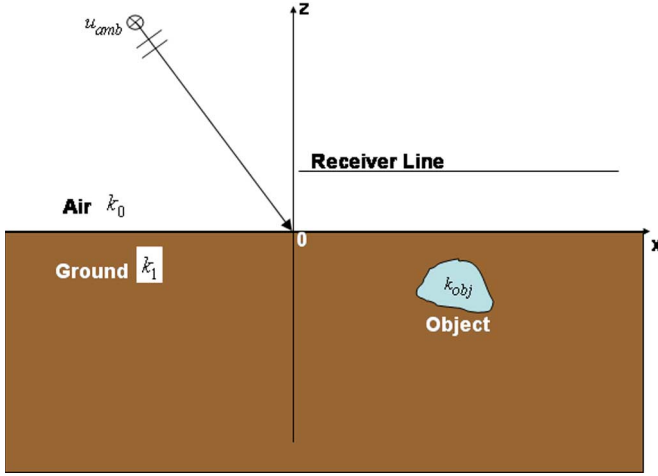


Fig. 1. GPR tomographic data collection setup for plane-wave incident radiation, with the object of interest being buried.

Appendix A derives a limiting result for the approximate Heaviside function used in Section III, whereas the explicit calculation of the Jacobian and Hessian matrices is given in Appendix B. Appendix C gives some salient features of the forward problem based on the method of moments, which is needed for the Jacobian and Hessian calculations.

## II. PROBLEM DEFINITION

### A. GPR Tomography Problem

The inverse scattering problem currently being considered is to recover the object's permittivity (denoted by  $\epsilon(\mathbf{r})$ ,  $\mathbf{r} \in \mathbb{R}^2$ ) and conductivity (denoted by  $\sigma(\mathbf{r}, \omega)$ ,  $\mathbf{r} \in \mathbb{R}^2$ ) distributions from the measurements at various angular frequencies  $\omega$  of the scattered field obtained from the interaction of an incident radiation with the object in question on a receiver surface outside the object. A schematic of a GPR tomography setup is shown in Fig. 1.

In the scalar approximation, the scattering process in GPR tomography is assumed to be modeled by the Helmholtz equation. The Helmholtz equation for the complex amplitude  $u(\mathbf{r}, \mathbf{r}_n, \omega)$ , at a point  $\mathbf{r} = (x, y, z)$  of a monochromatic wave of angular frequency  $\omega$ , due to a source at  $\mathbf{r}_n$ , propagating through a medium of complex wavenumber  $k(\mathbf{r}, \omega)$  is given by

$$\Delta u(\mathbf{r}, \mathbf{r}_n, \omega) + k^2(\mathbf{r}, \omega)u(\mathbf{r}, \mathbf{r}_n, \omega) = j_n(\mathbf{r}_n, \omega) \quad (2.1)$$

where  $\Delta$  is the Laplacian operator, and  $j_n(\mathbf{r}_n, \omega)$  is the assumed current distribution corresponding to the  $n$ th transmitter. The fields  $u(\mathbf{r}, \mathbf{r}_n, \omega)$  are assumed to be outgoing and satisfying the Sommerfeld radiation conditions at infinity. The complex wavenumber  $k(\mathbf{r}, \omega)$  is given by

$$k^2(\mathbf{r}, \omega) = \omega^2 \mu_0 \epsilon(\mathbf{r}) \left( 1 + i \frac{\sigma(\mathbf{r}, \omega)}{\omega \epsilon(\mathbf{r})} \right) \quad (2.2)$$

where  $\mu_0$  is the magnetic permeability of free space.

Define

$$f(\mathbf{r}) = \frac{k^2(\mathbf{r}, \omega) - k_{\text{amb}}^2(\mathbf{r}, \omega)}{k_{\text{amb}}^2(\mathbf{r}, \omega)} \quad (2.3)$$

with  $k(\mathbf{r}, \omega)$  being the wavenumber in the actual physical setting of the object(s) of interest embedded in an ambient medium corresponding to a wavenumber  $k_{\text{amb}}(\mathbf{r}, \omega)$ . In the present problem, the ambient medium comprises two half-spaces corresponding to air and ground, which are separated by an air-ground interface.

The independence of  $f(\mathbf{r})$  on  $\omega$  stems from the assumption that the quantity  $\tan \delta \equiv (\sigma(\mathbf{r}, \omega)/\omega \epsilon)$  does not vary with  $\omega$  in the frequency range of interest [19].

The reconstruction problem is thus the recovery of  $f(\mathbf{r})$  from the measurements at various angular frequencies  $\omega$  of the scattered field on the receiver surface. The total field is written as the sum of an incident ambient component  $u_{\text{amb}}(\mathbf{r}, \omega)$  and a scattered component  $u_{\text{sc}}(\mathbf{r}, \omega; f)$ , i.e.,

$$u(\mathbf{r}, \omega; f) = u_{\text{amb}}(\mathbf{r}, \omega) + u_{\text{sc}}(\mathbf{r}, \omega; f) \quad (2.4)$$

where

$$u_{\text{amb}}(\mathbf{r}, \omega) = \int_{V_s} g(\mathbf{r}, \mathbf{r}', \omega) j_n(\mathbf{r}') d\mathbf{r}' \quad (2.5)$$

and

$$u_{\text{sc}}(\mathbf{r}, \omega; f) = \int_{\Omega} g(\mathbf{r}, \mathbf{r}', \omega) (k_{\text{amb}}^2(\mathbf{r}', \omega) f(\mathbf{r}')) u(\mathbf{r}', \omega) d\mathbf{r}' \quad (2.6)$$

where  $V_s$  is the volume enclosing the source distribution, and  $\Omega$  is the object-domain volume. The Green function  $g(\mathbf{r}, \mathbf{r}', \omega)$  is the outgoing-wave solution of the equation

$$\Delta g(\mathbf{r}, \mathbf{r}', \omega) + k_{\text{amb}}^2(\mathbf{r}, \omega)g(\mathbf{r}, \mathbf{r}', \omega) = -\delta(\mathbf{r} - \mathbf{r}'). \quad (2.7)$$

The half-space Green function has been chosen for this paper [20], [21].

### B. Approximate Tomographic Reconstruction Problem

Observing that function  $f(\mathbf{r})$  contains information about the parameter values as well as the shape, we now express the parameter at a point in the image space as

$$f(\mathbf{r}) = f^g(\mathbf{r}) H_\rho[\phi(\mathbf{r})] \quad (2.8)$$

where field quantity  $f^g(\cdot)$  can be considered as a “ghost” parameter value since it manifests itself through the indicator function  $H_\rho[\phi(\cdot)]$  (the nomenclature is adopted in the spirit of the “ghost” field of the local shape function method of Chew *et al.* [22]).  $H_\rho[\cdot]$  is a Heaviside function taken in a suitable limiting sense defined as follows (as in [23]):

$$H_\rho(t) := \begin{cases} 0, & \text{if } t < -\rho \\ \frac{1}{2} \left\{ 1 + \frac{t}{\rho} + \frac{1}{\pi} \sin\left(\frac{\pi t}{\rho}\right) \right\}, & \text{if } t \in [-\rho, \rho] \\ 1, & \text{if } t > \rho. \end{cases} \quad (2.9)$$

Furthermore,  $\phi(\cdot)$  is a level-set-based representation of the image ([18] and references therein), with  $\{\mathbf{r} : \phi(\mathbf{r}) = 0\}$  representing the boundary  $\partial\Omega$  of the object(s) under consideration, which is supported in region  $\Omega$ . In this paper, without loss

of generality, we have considered the unknown object to be a single region; using level-set-based representations for multiple regions such as those mentioned in [13], the straightforward conceptual extension to those cases follows.

The level-set function can be defined as follows:

$$\phi(\mathbf{r}) = \begin{cases} d(\mathbf{r}, \partial\Omega), & \text{if } \mathbf{r} \in \Omega \\ -d(\mathbf{r}, \partial\Omega), & \text{if } \mathbf{r} \in \Omega^c \end{cases} \quad (2.10)$$

where  $d(\cdot)$  is a suitable distance measure.

Assume function  $f^g(\cdot)$  to be decomposed as [7], [9]

$$f^g(\mathbf{r}) = \sum_{i=1}^{N_b} \alpha_i \varsigma_i(\mathbf{r}) \quad (2.11)$$

where  $\alpha_i$  are the coefficients in a global basis  $\{\varsigma_i\}$ , and  $N_b$  are the number of basis vectors considered. For example,  $\{\varsigma_i\}$  can be considered to be a polynomial basis. Without loss of generality, in this paper, we consider only the zeroth-order term in this basis, i.e.,

$$f(\mathbf{r}) = \alpha H_p[\phi(\mathbf{r})] \quad (2.12)$$

where  $\alpha$  is the value of the unknown object electromagnetic parameter value. The choice of a single electromagnetic parameter value corresponds to the test case of a constant inhomogeneity in a constant background, which has been chosen without loss of generality to derive and numerically validate the algorithm. The important real-world aspect of nonhomogeneous background and/or object is implicit in this paper's formulation in that one needs to compute the incident fields for that background and express the unknown in basis containing more terms than just the constant term in the general representation (2.11).

Furthermore, define the closed boundary curve  $\{\mathbf{r} : \phi(\mathbf{r}) = 0\}$  as a parameterized (uniform B spline) curve [24]  $\Upsilon(s) = (x(s), z(s))$ , where for  $s \in [s_{\min}, s_{\max}]$

$$\Upsilon(s) = \sum_{q=1}^{M_s+1} N_{q,k}(s) \Upsilon_q^c \quad (2.13)$$

where  $\Upsilon_q^c = (x_q^c, z_q^c)$  are the control points. There are  $M_s + 1$  control points, and the  $N_{q,k}$  basis functions are of order  $k$  (degree  $k - 1$ );  $k$  must be at least 2 (linear) and at most  $M_s + 1$ , which is the number of control points. Since scaling or translating the knot vector has no effect on the shapes of the  $N_{q,k}$ , the knot vector determining the values of  $s$  at which the pieces of the curve join is written as  $[1, 2, \dots, k + M_s + 1]$ . For a closed curve, suppose that we have  $M_p$  points  $\Upsilon_1, \dots, \Upsilon_{M_p}$  defining the closed B spline. For a given order  $k$ , one will need  $M_p + k - 1$  control points (repeating the first  $k - 1$  points), i.e.,  $\Upsilon_1, \dots, \Upsilon_{M_p}, \Upsilon_1, \dots, \Upsilon_{k-1}$ , with the knot vector thus having  $M_p + 2k - 1$  uniformly spaced knots.

Hence, the closed boundary curve  $\Upsilon(s) = (x(s), z(s))$ , for  $s \in [s_{\min}, s_{\max}]$ , can be written as

$$\Upsilon(s) = \sum_{q=1}^{M_p} \tilde{N}_{q,k}(s) \Upsilon_q^c \quad (2.14)$$

where  $\tilde{N}_{q,k}(s) \equiv N_{q,k}(s) + N_{q_1,k}(s)$ , with  $q_1$  denoting the index corresponding to  $\Upsilon_q^c$  in the second (repeated) part of the control point sequence representing the closed boundary curve.

Define

$$\mathbf{h} = \begin{pmatrix} \text{Re}(\alpha) \\ \text{Im}(\alpha) \\ \mathbf{x}^c \\ \mathbf{z}^c \end{pmatrix}$$

where  $\alpha$ ,  $\mathbf{x}^c$ , and  $\mathbf{z}^c$  are the vectors with elements  $\{\alpha_i\}$ ,  $\{x_q^c | q = 1 \dots M_p\}$ , and  $\{z_q^c | q = 1 \dots M_p\}$ , respectively.

Recalling that we had defined the “approximate” tomographic imaging problem as one wherein the object shape, location, and an approximate (as against a more exact) estimate of the object's interior physical parameter values are reconstructed, this reconstruction problem can be defined as the solution to the following nonlinear minimum norm problem:

$$\begin{aligned} \min_{\mathbf{h}} \quad & \frac{1}{2} \|\mathbf{h} - \mathbf{c}\|^2 \\ \text{s.t.} \quad & \frac{1}{2} \|\zeta(\mathbf{h})\|^2 \quad \text{is minimal} \end{aligned} \quad (2.15)$$

where  $\mathbf{c}$  is a known constant representing an *a priori* information, which is typically taken to be the initial estimate of the iterative process (it can be changed within the iterative process to help stabilize the iterates), and

$$\zeta(\mathbf{h}) = \begin{pmatrix} \text{Re}(\mathbf{u}_{\text{data}} - \mathcal{A}(\mathbf{h})) \\ \text{Im}(\mathbf{u}_{\text{data}} - \mathcal{A}(\mathbf{h})) \end{pmatrix}$$

where  $\mathbf{u}_{\text{data}} (= \mathbf{u}^{\text{rec}} - \mathbf{u}_{\text{amb}}^{\text{rec}})$  is the “effective” measured data vector concatenated over the frequencies at which the measurements are taken,  $\mathbf{u}^{\text{rec}}$  is the measured field at the receiver, and  $\mathbf{u}_{\text{amb}}^{\text{rec}}$  is the ambient field that would have been measured at the receiver in the absence of the inhomogeneity. The functional  $\mathcal{A} : \mathbb{R}^N \rightarrow M/2$  is the measurement operator corresponding to the tomographic process, whose  $i$ th component (corresponding to the  $i$ th measurement) at the given frequency is  $\mathcal{A}^i(\mathbf{h}; \omega, \mathbf{r}^i) \equiv u_{\text{sc}}(\mathbf{r}^i, \omega; f)$  [as defined in (2.6)], with  $f(\mathbf{r}') = \alpha H[\phi(\mathbf{r}', \mathbf{h})]$ , where  $N$  is the length of vector  $\mathbf{h}$  and the number of measurements is  $M/2$  (for later notational convenience). The measurement operator is obtained via a suitable discretization scheme (in this paper, a method-of-moments scheme [21], [25] is applied to the integral equation of scattering) to solve the Helmholtz equation for the scattered fields, given the object parameters.

It must be noted that, as common practice, the problem (2.15) is chosen to approximate the actual ill-posed problem of solving for  $\mathbf{h}$ , i.e., the equation  $\mathcal{A}(\mathbf{h}) = \mathbf{u}_{\text{data}}$ . In this paper, the preceding minimization problem (2.15) is solved by using an iteratively regularized Gauss–Newton method (described in Section IV) that requires the computation of the Frechet derivatives of the received fields with respect to the parameter vector. This aspect is dealt with in the next section.

Note that the number of control points can also be considered as an implicit smoothing/regularization parameter. In realistic situations, one would have to solve a series of “surrogate”

inverse problems from a lesser number of control points to larger numbers (with the rank-deficient nature of the inverse problem becoming evident as the number of control points increases toward the actual number); each problem however has to be regularized separately due to its possible almost-rank-deficient nature. In this paper, we analyze the reconstructions in an almost-rank-deficient framework for an assumed fixed number of control points.

### III. FRECHET DERIVATIVES

#### A. Continuous-Domain Derivative

Define the residual  $\vartheta(f; \omega)$  in the continuous-domain representation of the unknown parameter  $f(x, z)$  at frequency  $\omega$  to be

$$\vartheta(f; \omega) = \mathbf{u}_{\text{data}}(\omega) - \mathcal{A}(f; \omega) \quad (3.1)$$

where the  $i$ th component of the measurement operator  $\mathcal{A}$  (corresponding to the  $i$ th measurement) at the given frequency is  $\mathcal{A}^i(f; \omega, \mathbf{r}^i) \equiv u_{\text{sc}}(\mathbf{r}^i, \omega; f)$  [as defined in (2.6)].

The Frechet derivative of the residual can thus be written as

$$\vartheta'(f) \delta f = \mathbf{v} \quad (3.2)$$

where the  $i$ th component of  $\mathbf{v}$  (corresponding to the  $i$ th receiver) is  $v_i \equiv v(\mathbf{r}^i, \omega)$ , with  $v(\mathbf{r}, \omega)$  being a solution of

$$\Delta v(\mathbf{r}, \omega) + k_{\text{nom}}^2 v(\mathbf{r}, \omega) = -k_{\text{amb}}^2 \delta f(\mathbf{r}) u(\mathbf{r}, \omega) \quad (3.3)$$

where  $\Delta$  is the Laplacian operator, and  $k_{\text{nom}}$  is the nominal wavenumber at the present iterate.

Thus, the solution for  $v_i := v(\mathbf{r}^i, \omega)$  in integral form would be

$$v(\mathbf{r}^i, \omega) = \int_{\Omega} g_B(\mathbf{r}^i, \mathbf{r}', \omega) (k_{\text{amb}}^2 \delta f(\mathbf{r}')) u(\mathbf{r}', \omega) d\mathbf{r}' \quad (3.4)$$

where  $g_B(\mathbf{r}^i, \mathbf{r}', \omega)$  is the Green function corresponding to the current parameter estimate being the ambient.

Thus, considering the object representation (2.12), we will have

$$\delta f(\mathbf{r}) = \alpha H'_\rho[\phi(\mathbf{r})] \delta \phi(\mathbf{r}) + H_\rho[\phi(\mathbf{r})] \delta \alpha \quad (3.5)$$

where  $H'_\rho[\cdot]$  denotes the derivative of the Heaviside function.

Observing from (2.9) that the support of  $H'_\rho[\phi(\mathbf{r})]$  is contained in  $\phi^{-1}[-\rho, \rho]$ , we can thus write (3.4) as

$$\begin{aligned} v(\mathbf{r}^i, \omega) = & \int_{\phi^{-1}[-\rho, \rho]} g_B(\mathbf{r}^i, \mathbf{r}', \omega) k_{\text{amb}}^2(\mathbf{r}', \omega) \\ & \times u(\mathbf{r}', \omega) \alpha H'_\rho[\phi(\mathbf{r}')] \delta \phi(\mathbf{r}') d\mathbf{r}' \\ & + \delta \alpha \int_{\Omega} g_B(\mathbf{r}^i, \mathbf{r}', \omega) k_{\text{amb}}^2(\mathbf{r}', \omega) \\ & \times u(\mathbf{r}', \omega) H_\rho[\phi(\mathbf{r}')] d\mathbf{r}'. \end{aligned} \quad (3.6)$$

We now define  $\mathbf{r}_b(\mathbf{r})$  as the unique boundary point corresponding to a point  $\mathbf{r}$  in the set  $\phi^{-1}[-\rho, \rho]$ . This uniqueness can be justified on the basis of the tubular neighborhood theorem [26], which says that, given any compact manifold  $\mathcal{M}$  embedded in Euclidean space, there is a neighborhood (called “tubular neighborhood”) around it such that, for any point  $\mathbf{r}$  in the tube, there is a unique point on  $\mathcal{M}$  closest to  $\mathbf{r}$ ; in our case,  $\mathcal{M}$  is a differentiable closed curve, and the Euclidean space is  $\mathbb{R}^2$ .

The tubular neighborhood theorem however is an existential result. For a plane curve such as in the 2-D problems under consideration, we can define the tube as consisting of all parallel curves  $\Upsilon^\lambda(s) = \Upsilon(s) + \lambda \hat{n}_{\text{sign}}(s)$  such that  $|\lambda \kappa_{\text{sign}}(s)| < 1$  for all values of  $s$ , where  $\kappa_{\text{sign}}(s)$  and  $\hat{n}_{\text{sign}}(s)$  are the signed curvature and the signed unit normal, respectively [27], [28]. This condition ensures that a parallel curve is regular and that the normal vectors of the curve  $\Upsilon(s)$  coincide with those of a parallel curve  $\Upsilon^\lambda(s)$  for all  $s$ . The Heaviside approximation parameter  $\rho$  can be taken as one such  $\lambda$ . Taking account of the spline curves under consideration in this paper, the Heaviside approximation parameter  $\rho$  is chosen as the least  $|\lambda_i|$  such that  $|\lambda_i \kappa_{\text{sign}}(s)| = 1/q'$  for some chosen  $q' > 1$  and for all values of  $s$  in segment  $i$  of the spline approximation. Note that the representation by parallel curves is for the signed-distance function, whereas the tubular neighborhood theorem is valid for an arbitrary level-set function. Furthermore, we draw attention to the fact [28] that a tube in three dimensions would be defined as consisting of all parallel surfaces  $\Upsilon^\lambda(x, y, z) = \Upsilon(x, y, z) + \lambda \hat{n}(x, y, z)$  such that  $|\lambda| < 1/C$ , where  $\hat{n}(x, y, z)$  is the standard unit normal and  $C$  is a positive constant greater than the absolute values of both the principal curvatures of the surface, thus ensuring generalizability of the Frechet derivative calculations here to 3-D, subject to the choice of a suitable basis representation for 3-D shapes.

Thus, with such a definition of the tube, we would have

$$\delta \phi(\mathbf{r}) = \delta \phi(\mathbf{r}_b(\mathbf{r})) \quad \text{if } \mathbf{r} \in \phi^{-1}[-\rho, \rho]. \quad (3.7)$$

Substituting (3.7) in (3.6), noting that  $\lim_{\rho \rightarrow 0} H'_\rho[\phi(\mathbf{r})] = (\delta[\phi(\mathbf{r})]/|\nabla \phi|)$  (see Appendix A for the proof), we have

$$\begin{aligned} \lim_{\rho \rightarrow 0} v_i(\mathbf{r}^i, \omega) = & \alpha \int_{\partial \Omega} g_B(\mathbf{r}^i, \mathbf{r}', \omega) k_{\text{amb}}^2(\mathbf{r}', \omega) \\ & \times u(\mathbf{r}', \omega) \left( \frac{-\nabla \phi \cdot \delta \mathbf{r}'}{|\nabla \phi|} \right) d\mathbf{r}' \\ & + \delta \alpha \int_{\Omega} g_B(\mathbf{r}^i, \mathbf{r}', \omega) k_{\text{amb}}^2(\mathbf{r}', \omega) \\ & \times u(\mathbf{r}', \omega) H[\phi(\mathbf{r}')] d\mathbf{r}' \end{aligned} \quad (3.8)$$

where  $H[\cdot]$  is the Heaviside function. To relate the present relations to those in [18], supposing we assume that  $\delta \alpha = 0$ , from the first term in the preceding expression and (3.5), we can write  $\delta f$  as a measure on  $\partial \Omega$  as follows:

$$\delta f(\mathbf{r}) = \alpha \left( \frac{-\nabla \phi \cdot \delta \mathbf{r}}{|\nabla \phi|} \right) \Big|_{\mathbf{r} \in \partial \Omega}. \quad (3.9)$$

Taking into account that the definitions of level-set function  $\phi(\cdot)$  in this paper are opposite in sign from those in [18], this expression for the relation between  $\delta f(\mathbf{r})$  and  $\delta \mathbf{r}$  is the same as [18, eq. (4)].

### B. Discrete-Domain Derivative

In this paper, we numerically solve the forward problem by the method of moments via a pulse-basis point-matching decomposition of the integral equation [21], [25] (the essential discretization steps have been mentioned in Appendix C). Assume basis decompositions of the following forms for parameter function  $f(\cdot)$  and field  $u(\cdot)$ :

$$f(\mathbf{r}) = \sum_{j=1}^n f_j \psi_j(\mathbf{r}) \quad u(\mathbf{r}, \omega) = \sum_{j=1}^n u_j(\omega) \psi_j(\mathbf{r}) \quad (3.10)$$

where  $n$  is the number of pixels in the image, and  $\{\psi_j(\mathbf{r})\}$  is an appropriate basis set; in our case, we choose it to be the pulse basis, i.e.,  $\psi_j(\mathbf{r}) = 1$  for  $\mathbf{r} \in \text{pixel } j$  and zero otherwise.

Assuming that a pulse-basis discretization in a method-of-moments framework is suitable for the coverage of the area covered by  $\delta f(\mathbf{r})$  in (3.4), it would follow that (3.6) could also be discretized via the same pulse basis.

Thus, in a pulse-basis discretization of  $\delta \phi(\mathbf{r})$  and  $u(\mathbf{r}', \omega)$ , we write the discrete approximation of (3.6) as

$$v_i = \sum_{j \ni (\mathbf{r}_j \in \phi^{-1}[-\rho, \rho])} G_B(i, j) u_j \{ \alpha H'_\rho[\phi_j] \} \delta \phi_j + \delta \alpha \sum_j G_B(i, j) u_j H_\rho[\phi_j] \quad (3.11)$$

where  $\phi_j = \phi(\mathbf{r}_j)$ , and

$$G_B(i, j) = \int_{\Omega} g_B(\mathbf{r}^i, \mathbf{r}', \omega) k_{\text{amb}}^2(\mathbf{r}', \omega) \psi_j(\mathbf{r}') d\mathbf{r}' \quad (3.12)$$

where the  $\omega$  dependence in  $G_B(i, j)$  (on the left-hand side) has been suppressed for ease of notation.

Using the equivalence of the distorted-Born and Newton–Kantorovich formulations [1], denoting  $\delta \vartheta_i := v_i$ , we can write

$$\delta \vartheta_i = \sum_{j \ni (\mathbf{r}_j \in \phi^{-1}[-\rho, \rho])} \frac{\partial \vartheta_i}{\partial f_j} \{ \alpha H'_\rho[\phi_j] \} \delta \phi_j + \sum_j \frac{\partial \vartheta_i}{\partial f_j} H_\rho[\phi_j] \delta \alpha \quad (3.13)$$

where relations for  $(\partial \vartheta_i / \partial f_j)$  are shown in Appendix C.

Thus, substituting (3.7) in (3.13), we have

$$\delta \vartheta_i = \sum_{j_\rho} \frac{\partial \vartheta_i}{\partial f_j} \{ \alpha H'_\rho[\phi_j] \} (-\nabla \phi \cdot \delta \mathbf{r}_b^j) + \sum_j \frac{\partial \vartheta_i}{\partial f_j} H_\rho[\phi_j] \delta \alpha \quad (3.14)$$

where  $\mathbf{r}_b^j = \mathbf{r}_b(\mathbf{r}_j)$ ,  $j_\rho \equiv \{j \ni (\mathbf{r}_j \in \phi^{-1}[-\rho, \rho])\}$ , and we have used the level-set propagation condition [18] (i.e.,  $\delta \phi + \nabla \phi \cdot \delta \mathbf{r} = 0$ ) that is satisfied on the boundary.

Recalling the B-spline representation of the boundary curve (2.14), since  $\mathbf{r}_b^j = \Upsilon(s_j)$  for some  $s_j \in [s_{\min}, s_{\max}]$ , we will have

$$\delta \mathbf{r}_b^j \equiv \delta \Upsilon(s_j) = \sum_{q=1}^{M_p} \tilde{N}_{q,k}(s_j) \delta \Upsilon_q^c. \quad (3.15)$$

Thus, we have the variation of the measured scattered fields w.r.t variation in the control points (of the boundary curve) and the inhomogeneity to be

$$\delta \vartheta_i = \sum_{j_\rho} \frac{\partial \vartheta_i}{\partial f_j} \{ \alpha H'_\rho[\phi_j] \} \left( -\nabla \phi \cdot \left( \sum_{q=1}^{M_p} \tilde{N}_{q,k}(s_j) \delta \Upsilon_q^c \right) \right) + \sum_j \frac{\partial \vartheta_i}{\partial f_j} H_\rho[\phi_j] \delta \alpha \quad (3.16)$$

where we will have, for  $i = 1, \dots, M/2$ ,  $\delta \zeta_i = \text{Re}(\delta \vartheta_i)$  and  $\delta \zeta_{i+M/2} = \text{Im}(\delta \vartheta_i)$ . The explicit calculation of this expression for the Frechet derivative is given in Appendix B.

## IV. SCHEME OF RECONSTRUCTION AND ANALYSIS

### A. Basic DTRGN Scheme

Recall from Section II that the approximate tomographic problem to be solved is the minimum c-norm problem (2.15). To solve this problem, a scheme based on an iteratively regularized Gauss–Newton approximation is utilized. The multifrequency GPR tomography problem under consideration in this paper is found to have an almost-rank-deficient Jacobian matrix  $\mathbf{J}(\mathbf{h})$  at the solution point of  $\zeta(\mathbf{h}) \simeq 0$ . It is well known that the Gauss–Newton method [29] is a very efficient approach for many parameter estimation problems. However, for ill-conditioned objective functionals [such as the unregularized functional  $(\|\zeta(\mathbf{h})\|^2/2)$ ] found in many inverse problems, first-order methods such as the Gauss–Newton will not converge due to the rank deficiency of the Jacobian matrix. Using iterated Tikhonov regularization, a stable solution may be found, which greatly improves the condition of the problem and also the convergence rate over the Gauss–Newton method applied to the unregularized functional.

The generic Tikhonov-regularized (with regularization parameter  $\mu$ ) nonlinear least squares problem corresponding to (2.15) is

$$\min_{\mathbf{h}} \frac{1}{2} \|\zeta_{\text{aug}}(\mathbf{h}; \mu)\|^2 \quad (4.1)$$

where

$$\zeta_{\text{aug}}(\mathbf{h}; \mu) \equiv \begin{pmatrix} \zeta(\mathbf{h}) \\ \mu(\mathbf{h} - \mathbf{c}) \end{pmatrix}.$$

The basic idea with regularization is to find an acceptable solution within a certain region since one can find acceptable

solutions to the original problem (without regularization) in many parts of the solution space. Thus, “c” should be interpreted as the center of such a region, and regularization parameter  $\mu$  typically reflects the (2-norm) size of this region.

However, a main problem with the problem (4.1) is the selection of regularization parameter  $\mu$ . Typically, in the literature, two approaches have been followed to regularize the problem (2.15) via the use of Tikhonov functionals. The first one is of selecting parameter  $\mu$  in (4.1) based on *a posteriori* (discrepancy-principle-based) parameter rules. These have the computational pitfall of requiring testing a sequence of regularization parameters to find a minimizer fulfilling the discrepancy principle, for each of which the minimizer of the nonlinear Tikhonov functional [(4.1)] has to be evaluated. To avoid this pitfall, one can use iteratively regularized optimization methods, which update the regularization parameter with the iterations, in steepest-descent-based schemes [30], [31] or Newton-type methods [2], [3], [14], [30], [32], [33]. In this paper, we follow the latter class of methods in using a Gauss–Newton-based iterative regularization approach to solve the minimum norm problem (2.15).

Basically, we are solving approximately a sequence of Tikhonov-regularized nonlinear least squares problems ( $\min_{\mathbf{h}} \zeta_{\text{aug}}(\mathbf{h}; \mu_t)$ ) for a fixed center  $\mathbf{c}$  and a sequence of decreasing regularization parameters  $\mu_t$ . The approximate solution  $\mathbf{h}(\mu_t)$  of one such subproblem is taken as the starting point of the next subproblem with regularization parameter  $\mu_{t+1} < \mu_t$ . The Gauss–Newton method is used to compute an approximate solution for this kind of subproblem. In the rest of this paper, for ease of notation, we use  $\mu$ , instead of  $\mu_t$ .

In practical applications, numerical experience allows us to take the approximate solution of a subproblem to be the minimum of the linear-residual approximation to that objective function.<sup>2</sup> Recalling that the Gauss–Newton method goes to the minimum of such a quadratic objective function in one iteration, we use a computationally inexpensive approach of checking at each iteration whether to reduce the regularization parameter or not, depending on whether, at that iterate, the first-order model is a good-enough approximation of the actual residual. If the step length is 1, i.e., a full step has been taken, it is assumed that the first-order model is good enough. It is important to note that, by decreasing  $\mu$ , what is actually done is changing the optimization problem to one that is less smooth (i.e., to a more rapidly varying objective functional).

Regularization parameter  $\mu$  is a smoothing factor (should be larger than the noise), and a larger  $\mu$  gives an easier optimization problem to solve. A large (small)  $\mu$  gives a solution close to (away from) “c.” As will also be seen later via the analysis, too small a  $\mu$  results in the Gauss–Newton method not converging. Hence, it is important to start the algorithm with a large  $\mu$ , so that the iterates do not get driven too far from “c” initially. During iterations,  $\mu$  should be decreased (never increased, however, for that c) in order to find lower minima. Observe that this will lead to a solution further away from “c.”

Note that the proposed method is, in its basic form, different from the Levenberg–Marquardt method. It is a Gauss–Newton method applied on a regularized problem. In addition, if the “c” is adjusted in each iteration, then we have a method similar to the Levenberg–Marquardt [30], whereas, in our case, the center “c” is only changed if convergence problems occur close to the solution.

To solve this problem, an iterative scheme based on the Gauss–Newton approximation solves, at the current iterate  $\mathbf{h}$

$$\min_{\mathbf{p}} \left\| \begin{pmatrix} \mathbf{J}(\mathbf{h})\mathbf{p} + \zeta(\mathbf{h}) \\ \mu(\mathbf{h} - \mathbf{c} + \mathbf{p}) \end{pmatrix} \right\|^2 \quad (4.2)$$

where the  $M \times N$  matrix  $\mathbf{J}(\mathbf{h})$  is the Jacobian matrix of the functional  $\zeta(\mathbf{h})$  with respect to  $\mathbf{h}$ , which is defined via a Taylor series expansion of the form

$$\zeta(\mathbf{h} + \mathbf{p}) = \zeta(\mathbf{h}) + \mathbf{J}(\mathbf{h})\mathbf{p} + \mathcal{O}(\|\mathbf{p}\|^2). \quad (4.3)$$

The next iterate is given by

$$\mathbf{h}^{k+1} = \mathbf{h}^k + \beta_k \mathbf{p}^k \quad (4.4)$$

where step length  $\beta_k$  is chosen via line search such that the objective functional is sufficiently reduced. The search direction  $\mathbf{p}^k$  computed from (4.2) can be written as

$$\mathbf{p}^k = -\mathbf{B}(\mathbf{h}^k) \begin{pmatrix} \zeta(\mathbf{h}^k) \\ \mathbf{h}^k - \mathbf{c} \end{pmatrix} \quad (4.5)$$

where

$$\mathbf{B}_k \equiv \mathbf{B}(\mathbf{h}^k) = \left( (\mathbf{J}_k^T \mathbf{J}_k + \mu^2 \mathbf{I})^{-1} \mathbf{J}_k^T \middle| \mu^2 (\mathbf{J}_k^T \mathbf{J}_k + \mu^2 \mathbf{I})^{-1} \right) \quad (4.6)$$

where we do not explicitly form the product  $\mathbf{J}_k^T \mathbf{J}_k$  in the computation of matrix  $\mathbf{B}_k$  for reasons of numerical stability; it is computed via the singular value decomposition of  $\mathbf{J}_k$ .

Thus, the method employed in our work is a DTRGN method with line search; for ease of nomenclature, we only say the DTRGN method. We call it differently from “iteratively regularized Gauss–Newton” since our approach in the choice of parameters as well as the methodology of analysis is different from the methods described in [30]. In addition, our scheme for the changing of the regularization parameter is different from those of [3] and [33] in that we link the line search with the change of  $\mu$ , whereas, in their work,  $\mu$  is, in effect, varied proportional to the norm of the residual  $\zeta$  (with a proportionality constant that depends on the type of data used and needs to be set via numerical implementation).

The termination criterion that we have used is a relative one, i.e., we measure “how much” of the residual remains to minimize. The relative criterion is defined as

$$\epsilon_{\text{rel}} = \frac{\|\mathcal{P}_{\mathbf{J}_{\text{aug}}}\|}{\|\zeta_{\text{aug}}\|} \quad (4.7)$$

<sup>2</sup>Note that the objective function is proportional to the squared norm of the residual.

where  $\mathcal{P}_{\mathbf{J}_{\text{aug}}}$  is the orthogonal projection onto the range space of  $\mathbf{J}_{\text{aug}}$ , and

$$\mathbf{J}_{\text{aug}} = \begin{pmatrix} \mathbf{J}(\mathbf{h}) \\ \mu \mathbf{I}_N \end{pmatrix}.$$

Termination of the nonlinear recursive scheme is set as the satisfaction of the criterion  $\epsilon_{\text{rel}} < \text{tol}$  for some tolerance limit  $\text{tol}$  or the iterates staying stable.

In practice, it is very difficult to know whether we have stopped at a correct solution and a correspondingly “optimal”  $\mu$ . We mention that, in a regularization approach close to the spirit of ours, the seminal work in [31] combines the minimization of the Tikhonov functional with a steepest descent scheme and derives global convergence under certain smoothness criteria on the true solution. However, those criteria are very difficult to be tested in typical test problems (they have solved a Single Photon Emission Computed Tomography problem in medical imaging); in test cases, they can only tentatively state that the regularization parameter seems to be stopping at a good value. This is only to point out the level of difficulty in obtaining applicable convergence results in all such algorithms. Hence, in our work, assuming that we are close to that “optimal”  $\mu$ , based on a local convergence analysis using Hessian information, we apply a methodology of numerically checking the iterates for convergence.

### B. Local Convergence of the DTRGN Scheme

The Tikhonov-regularized Gauss–Newton scheme is locally analyzed (using second-order information) for convergence by evaluating an iteration matrix at the current iterate and subproblem (characterized by a particular value of  $\mu$ ), which is then subsequently decomposed to yield *distinct* contributions to the rate of convergence from various sources. The objectives of this analysis are to numerically attempt to: 1) confirm whether an iterate sequence is part of a convergent subsequence and 2) (if not convergent) yield the contribution to nonconvergence from respective convergences in data and parameter spaces as well as from choices of the regularization parameter.

Close to the solution  $\mathbf{h}^*$ , the convergence is generally linear, and we can write [2], [14]

$$\mathbf{h}^{k+1} - \mathbf{h}^* = \mathbf{K}(\mathbf{h}^k)(\mathbf{h}^k - \mathbf{h}^*) + \text{second-order terms} \quad (4.8)$$

where

$$\mathbf{K}(\mathbf{h}^k) = -(\mathbf{J}_k^T \mathbf{J}_k + \mu^2 \mathbf{I})^{-1} (\mathbf{H}^T \odot \boldsymbol{\zeta}) \quad (4.9)$$

where  $\mathbf{H}^T \equiv (\mathbf{H}_1^T, \dots, \mathbf{H}_m^T)$ , with  $\mathbf{H}_i = \boldsymbol{\zeta}_i''(\mathbf{h}^k)$  being the Hessian matrix corresponding to the  $i$ th measurement, and the “inner product”  $\odot$  is defined as  $\mathbf{H}^T \odot \mathbf{q} = \sum_i \mathbf{H}_i^T q_i$ . The Hessian matrices in this paper are explicitly calculated in Appendix B. In the rest of this section, we drop the subscript  $k$  for ease of notation.

The spectral radius of the local iteration matrix  $\mathbf{K}(\mathbf{h}^k)$  determines the rate of convergence. Denoting  $\varrho(\mathbf{A})$  as the spectral radius of matrix  $\mathbf{A}$  (i.e., the maximum of the absolute values of

the eigenvalues of  $\mathbf{A}$ ), the convergence condition can thus be written as

$$\text{GN converges} \Rightarrow \varrho(\mathbf{K}) < 1 \Leftrightarrow \text{Strong loc. min.}$$

$$\text{GN diverges} \Rightarrow \varrho(\mathbf{K}) > 1 \Leftrightarrow \text{Saddlepoint.} \quad (4.10)$$

Note, however, that knowledge of  $\varrho(\mathbf{K})$  does not give us an insight into sources of possible nonconvergence of the iterations. To gain that insight, we further decompose the iteration matrix into data and parameter space components. In order to do this, we define the singular value decomposition of the Jacobian matrix  $\mathbf{J}$  in the form  $\mathbf{J} = \mathbf{J}_1 + \mathbf{J}_2$  as follows:

$$\mathbf{J} = \mathbf{U} \mathbf{S} \mathbf{V}^T = (\mathbf{U}_1, \mathbf{U}_2) \text{diag}(\mathbf{S}_1, \mathbf{S}_2) (\mathbf{V}_1, \mathbf{V}_2)^T \quad (4.11)$$

with  $\mathbf{S}_1 = \text{diag}(s_1, \dots, s_r)$  and  $\mathbf{S}_2 = \text{diag}(s_{r+1}, \dots, s_n)$ , where  $r$  is a rank of interest at a particular iteration, which is usually considered as the number of singular values above the value of  $\mu$ .

Splitting  $(\mathbf{J}^T \mathbf{J} + \mu^2 \mathbf{I})^{-1}$  into terms corresponding to the subspaces defined by the assumed value of  $r$ , we have

$$\begin{aligned} \mu^2 (\mathbf{J}^T \mathbf{J} + \mu^2 \mathbf{I})^{-1} &= \mu^2 \mathbf{V}_1 \mathbf{S}_{V1} \mathbf{V}_1^T + \mathbf{V}_2 \mathbf{S}_{V2} \mathbf{V}_2^T \\ &\equiv \mu^2 \mathbf{E}(\mu) + \mathbf{N}(\mu) \end{aligned} \quad (4.12)$$

where  $\mathbf{S}_{V1} = \text{diag}\{1/[s_1^2(1+(\mu/s_1)^2)], \dots, 1/[s_r^2(1+(\mu/s_r)^2)]\}$ , and  $\mathbf{S}_{V2} = \text{diag}\{1/[1+(s_{r+1}/\mu)^2], \dots, 1/[1+(s_n/\mu)^2]\}$ .

Thus, substituting (4.12) in (4.9), we further obtain [2], [14]

$$\mathbf{K}(\mathbf{h}) = \mathbf{K}_1(\mathbf{h}) + \mathbf{K}_2(\mathbf{h}) + \mathbf{K}_3(\mathbf{h}) + \mathbf{K}_4(\mathbf{h}) \quad (4.13)$$

where

$$\mathbf{K}_1(\mathbf{h}) = -\mathbf{E}(\mu) (\mathbf{H}^T \odot \mathcal{P}_{S1} \boldsymbol{\zeta}) \quad (4.14)$$

$$\mathbf{K}_2(\mathbf{h}) = \mathbf{N}(\mu) \left( \mathbf{H}^T \odot (\mathbf{J}_1^\dagger)^T (\mathbf{h} - \mathbf{c}) \right) \quad (4.15)$$

$$\mathbf{K}_3(\mathbf{h}) = \mu^2 \mathbf{E}(\mu) \left( \mathbf{H}^T \odot (\mathbf{J}_1^\dagger)^T (\mathbf{h} - \mathbf{c}) \right) \quad (4.16)$$

$$\mathbf{K}_4(\mathbf{h}) = -\frac{1}{\mu^2} \mathbf{N}(\mu) (\mathbf{H}^T \odot \mathcal{P}_{S1} \boldsymbol{\zeta}) \quad (4.17)$$

where  $S_1 = \text{Null-space}(\mathbf{J}_1^T)$ ,  $\mathcal{P}_{S1}$  is the orthogonal projector onto  $S_1$ , and  $\mathbf{J}_1^\dagger$  is the Moore–Penrose pseudoinverse of  $\mathbf{J}_1$ .

In the preceding expression for  $\mathbf{K}(\mathbf{h})$ , we observe that the first two terms mainly correspond to the errors due to the normal curvatures in the objective function and parameter spaces, respectively. The third (fourth) term is usually heavily dependent on regularization parameter  $\mu$  and the residual in the parameter space (objective function space); the third term is typically small when close to convergence (since convergence usually implies that  $\mu$  is small enough), and the fourth term limits the decrease in the value of the regularization parameter. This observation (by inspection of  $\mathbf{K}_4$ ) that  $\mu$  cannot be too small at convergence is corroborated by the commonly observed fact that too small a  $\mu$  leads to poor reconstruction quality as well



as by the analysis for the steepest-descent-based regularization method in [31]. This also points to a minimum value of  $\mu$  below which the decreasing sequence of  $\{\mu_t\}$  should not fall (and thus to a corresponding underlying limiting cost functional) in order to ensure the stability of the iteration process.

Thus, the utility of the nature of the decomposition (4.13) is evident, in that, rather than having only the total iteration matrix (and its spectral radius), which would be typically available (and would not give us any insight into the *sources* of nonconvergence), we now have information regarding the *separate* effects of the objective function and parameter space errors, as well as those of the regularization parameter, on the convergence of the iterates.

It can be seen that  $\varrho(\mathbf{K}_1)$  reflects the convergence factor for the Gauss–Newton method in the full rank case without regularization [34]. Thus, it basically measures the size of the residual  $\zeta$  and the normal curvature of functional space.  $\varrho(\mathbf{K}_2)$  reflects the size of the residual “ $\mathbf{h} - \mathbf{c}$ ” and the curvature in the parameter space (and not in the functional space, as for  $\varrho(\mathbf{K}_1)$ ). Thus, if  $\varrho(\mathbf{K}_2) > 1$ , the residual “ $\mathbf{h} - \mathbf{c}$ ” is too large or the problem is probably too nonlinear. The solutions to this issue would be to either change the center  $\mathbf{c}$  during the iteration (but not too often since we could drift away from the region of interest) or to change the mathematical model to a less nonlinear formulation.

The analysis is used to check whether, at the point of stopping, the iterate is part of a convergent subsequence or not by checking if  $\varrho(\mathbf{K}) < 1$  (as well as the individual  $\varrho(\mathbf{K}_i)$ , to have a stricter bound). If so, then, that iterate is taken as the final one. If not, then, the source of nonconvergence is sought to be located by using  $\varrho(\mathbf{K}_i)$  typically as follows: If convergence is not reached for a certain  $\mu$ , then,  $\varrho(\mathbf{K}_2)$  or  $\varrho(\mathbf{K}_4)$  is often too large. There is nothing to do about  $\mathbf{K}_4$  since we do not want to increase  $\mu$  for that  $\mathbf{c}$ . Instead, we can change the center  $\mathbf{c}$  and thereby greatly reduce  $\varrho(\mathbf{K}_2)$ , which improves the situation unless  $\varrho(\mathbf{K}_4)$  is still too large. Of course, if the estimate has indeed reached a good termination point, we have seen, in the course of several simulational runs, that the value of  $\varrho(\mathbf{K}_1)$  stays stable across the  $\mathbf{c}$  change; if not, we found that choosing the estimate with lesser  $\varrho(\mathbf{K}_1)$  yields a better reconstruction. In addition, the criterion of the stability of  $\varrho(\mathbf{K}_1)$  across a  $\mathbf{c}$  change has been found to help choose a stopping iterate from an unstable sequence, as shown in the analysis of reconstructions from some noisier data sets.

It must be noted that it is not the case that  $\varrho(\mathbf{K}) = \sum_i \varrho(\mathbf{K}_i)$ . However, the decomposition (4.13) separates (otherwise unified) error sources, as previously explained. In addition, considering that  $\varrho(\mathbf{K}) < 1$  implies the convergence of the Gauss–Newton method, along with our observation in a variety of problems that, typically,  $\varrho(\mathbf{K}) \leq \sum_i \varrho(\mathbf{K}_i)$  and/or the overall  $\varrho(\mathbf{K})$  is of similar magnitude as the largest  $\varrho(\mathbf{K}_i)$  (as shown in Tables III and IV in the next section), the study of  $\mathbf{K}_i$  gives important insights into the sources of nonconvergence of the regularization scheme. This insight gives hints about which kinds of changes are needed to get convergence for the Gauss–Newton method. In the examples presented in our study, we have indeed either arrived at a point where  $\varrho(\mathbf{K}) < 1$  by simply using the termination criterion (4.7) or

used the information gained from the analysis to arrive at such an iterate (where  $\varrho(\mathbf{K}) < 1$ ), as previously explained and also numerically shown in the studies presented in Section V.

The overall algorithm including the reconstruction and analysis phases has been provided here.

### I Initialization

(a) Estimate  $\mathbf{h}^0$ , the “best-fit” circular object within the Born approximation according to (5.1).

(b)  $\mathbf{c} := \mathbf{h}^0$ , with  $\mu$  set at a suitable “large” value (less than one).

### II Reconstruction phase

For  $k = 1, 2, \dots$ , until  $\epsilon_{\text{rel}} < \text{tol}$  or the residual is unchanging for many past  $k$ ,

(a) Estimate the Heaviside approximation parameter  $\rho$  (as explained in the paragraph prior to (3.7)), such that  $|\rho \kappa_{\text{sign}}(s)| < 1$ ,  $s \in [s_{\min}, s_{\max}]$ , and evaluate the Jacobian  $\mathbf{J}(\mathbf{h}^k)$  using (B1)–(B3).

(b) Solve (4.2) for  $\mathbf{p}^k$ .

(c) Do a line search to find  $\beta_k$ .

(d) If  $\beta_k \simeq 1$ , then,  $\mu := \mu/q$ , for a suitable choice of  $q > 1$  (we chose  $q = 2$ ).

(e)  $\mathbf{h}^{k+1} = \mathbf{h}^k + \beta_k \mathbf{p}^k$ .

### III Analysis phase

Check whether the terminal iterate is part of a convergent subsequence by checking if  $\varrho(\mathbf{K}) < 1$ ; if not, use evaluations of  $\varrho(\mathbf{K}_i)$ ,  $i = 1, \dots, 4$ , close to the termination point to locate and rectify the source of nonconvergence (as explained in Sections IV and V).

## V. NUMERICAL STUDIES

### A. Test Cases and Reconstruction Aspects

Numerical studies have been carried out on the reconstruction and analysis problem of small dielectric minelike objects of different shapes for various noise conditions. Scattered data at multiple frequencies (0.7, 0.9, 1.1, and 1.3 GHz) and multiple-angle plane-wave incidence (15 angles in  $[-\pi/3, \pi/3]$ ) are used in our studies. Data sets have been simulated by adding Gaussian random noise of different variances to the exact data. In these studies, the data are collected on a line 10 cm above the ground, and at each frequency, 120 data points are considered from  $x = -24$  cm to  $x = 24$  cm. The subsurface reconstruction domain considered is  $16 \times 16$  cm ( $x = -8$  cm,  $\dots$ , 8 cm and  $z = -0.4$  cm,  $\dots$ ,  $-16.4$  cm). In the method-of-moments discretization of the reconstruction domain, we use a grid measuring  $40 \times 40$ . In this paper, cubic splines have been used (i.e., the order of the spline representation is  $k = 4$ ), and the number of distinct control points  $M_p$  considered is eight.

The test cases are specified by 1) material composition, i.e., P1 and P2, whose specifications are given in Table I; 2) shapes S1 and S2; and 3) noise levels denoted by N1 and N2, which were formed by adding Gaussian noise of zero mean and standard deviation of 0.1 and 0.2 times the maximum absolute value of the exact data set, respectively. Hence, the various phantoms are specified as S1P1N1, S1P1N2,  $\dots$ , S2P2N2.

The initialization of the recursive scheme is done by estimating a circular homogeneous object that best generates the

TABLE I  
 TEST CASE MATERIAL SETTINGS

Notation	Ambient ( $\epsilon_r, \tan \delta$ )	Object ( $\epsilon_r, \tan \delta, f$ )
P1	Dry sand, (2.55, 0.0282)	(4.24, 0.0636, $0.6644 + i0.0588$ )
P2	Wet sand (4.5, 0.03)	(10, 0.01797, $1.2221 - i0.02667$ )

measured data under the Born approximation. Since the linearized scattering equation may not truly represent the scattering process, a constraint is applied on the maximum magnitude of reconstructed values of object inhomogeneity parameters to ensure that the object is within the validity of the Born approximation; in this paper, we have set  $|\alpha| < 0.6$  for the starting estimate. We define

$$\tilde{\mathbf{h}} = \begin{pmatrix} \text{Re}(\alpha) \\ \text{Im}(\alpha) \\ x_{\text{center}} \\ z_{\text{center}} \\ R \end{pmatrix}$$

with  $(x_{\text{center}}, z_{\text{center}}) \equiv \mathbf{r}_c$  and  $R$  being the center coordinates and radius of the object, respectively.

Hence, an estimate of the “best-fit” circular object within the Born approximation can be obtained as

$$\min_{\tilde{\mathbf{h}} \in \mathbf{D}} \left\| \zeta^{\text{Born}}(\tilde{\mathbf{h}}) \right\|^2 \quad (5.1)$$

where  $\mathbf{D}$  represents assumed box bounds for the various unknowns

$$\zeta^{\text{Born}}(\tilde{\mathbf{h}}) = \begin{pmatrix} \text{Re}(\mathbf{u}_{\text{data}} - \mathcal{A}^{\text{Born}}(\tilde{\mathbf{h}})) \\ \text{Im}(\mathbf{u}_{\text{data}} - \mathcal{A}^{\text{Born}}(\tilde{\mathbf{h}})) \end{pmatrix}$$

where  $\mathcal{A}^{\text{Born}}(\tilde{\mathbf{h}})$  is the scattered field under the Born approximation and is obtained from  $\mathcal{A}(\tilde{\mathbf{h}})$  [as defined after (2.15)] by replacing  $u(\mathbf{r}', \omega, \tilde{\mathbf{h}})$  with  $u_{\text{amb}}(\mathbf{r}', \omega)$  in the integrand and noting that the level-set function for an object with a circular boundary can be evaluated as

$$\phi(\mathbf{r}', \tilde{\mathbf{h}}) = R - \|\mathbf{r}' - \mathbf{r}_c\|. \quad (5.2)$$

The approximation to the Heaviside function used for the evaluation of this first estimate is  $H[\cdot] \simeq H_\rho[\cdot]$ , where  $\rho$  has been set as the method-of-moments’ grid-discretization interval for the initialization step to ensure a gradual slope. In this paper, this nonlinear minimization problem for the starting estimate is solved by using the Matlab routine “lsqnonlin” (since a rough starting estimate is what we need; however, this function is not used in the Gauss–Newton iterations). The initial control points of the full nonlinear scheme are distributed along the perimeter of this initial circular object. Typically, in our initial estimate, we set the imaginary part of the inhomogeneity parameter  $\alpha$  to zero.

As mentioned in Section III, in the course of the solution of the full nonlinear reconstruction problem (4.1), at each iteration, the Heaviside approximation parameter  $\rho$  is chosen as the

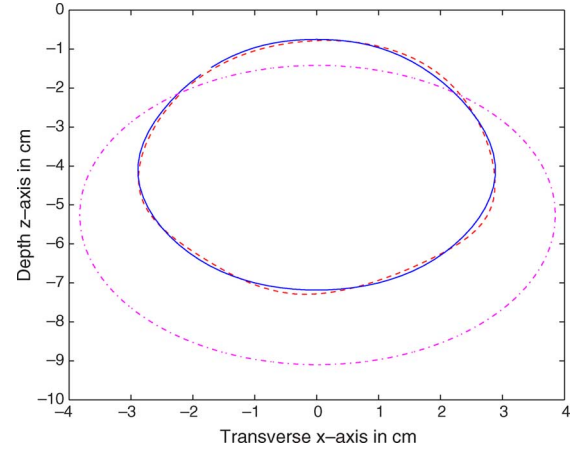


Fig. 2. Phantom S1P1N1 (data SNR = 34.53865 dB) (solid line: actual shape, dotted line: reconstructed shape; dot-dashed line: first estimate). Reconstructed  $f = 0.66378 + i 0.05474$ , and actual  $f = 0.6644 + i 0.0588$ .

least  $|\lambda_i|$  such that  $|\lambda_i \kappa_{\text{sign}}(s)| = 1/q'$  for some chosen  $q' > 1$  and for all values of  $s$  in segment  $i$  of the spline approximation, where  $\kappa_{\text{sign}}(s)$  and  $\hat{n}_{\text{sign}}(s)$  are the signed curvature and the signed unit normal, respectively.

The initial value of vector  $\mathbf{c}$  is set at the initial estimate. Since the chosen  $\mathbf{c}$  value is in the nature of an *a priori* information, during the iterations, it needs to be such that the regularization region is well represented in order for the iterates to stabilize and/or the termination criterion (4.7) to be achieved. A further discussion about the choice of  $\mathbf{c}$  is found in the subsequent section on the second-order analysis.

In the nonlinear regularization scheme [described by (4.4)–(4.6)], the setting of regularization parameter  $\mu$  is done by initializing it to a suitably “large” value and then reducing it in steps corresponding to a reduction in the objective function value in the line search step, when the step size is large enough (i.e., the step size should be close to 1). Termination of the nonlinear recursive scheme was set as the satisfaction of the criterion  $\epsilon_{\text{rel}} < 0.01$  and/or the iterates staying stable. To verify the convergence of these estimates, the iterates close to termination have been subjected to the second-order analysis, as shown in the next section.

Reconstructions for the eight test cases are shown in Figs. 2–9. The values of the reconstructed electrical parameters are given in the figure captions. The reconstructed electrical parameters are also given in Table II. As we observe, in addition to the good correspondence of reconstructed and actual shapes, there is a good agreement between the real and imaginary parts of the reconstructed values of the electrical parameter  $f(\mathbf{r}) (= \alpha)$ , and the actual values, for the test cases considered.

Aside from the obvious reduction in computational effort over the full pixel-basis reconstructions in the inversion part of the optimization scheme due to the constraining of the solution space, we see, from (3.16), that, since the number of control points and the number of pixels in the tube are typically very much smaller than the number of pixels in the support of the present object at that iterate, the main computational effort in the forward problem is (as for a pixel-based reconstruction scheme) in computing the pixel-basis Jacobian. However, since

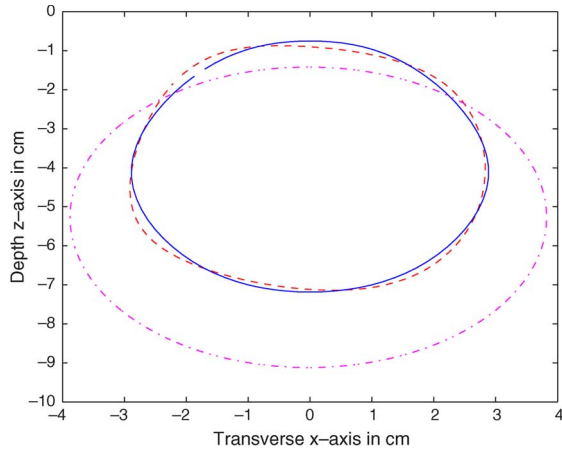


Fig. 3. Phantom S1P1N2 (data SNR = 20.66664 dB) (solid line: actual shape, dotted line: reconstructed shape; dot-dashed line: first estimate). Reconstructed  $f = 0.656123 + i 0.058301$ , and  $f = 0.6644 + i 0.0588$ .

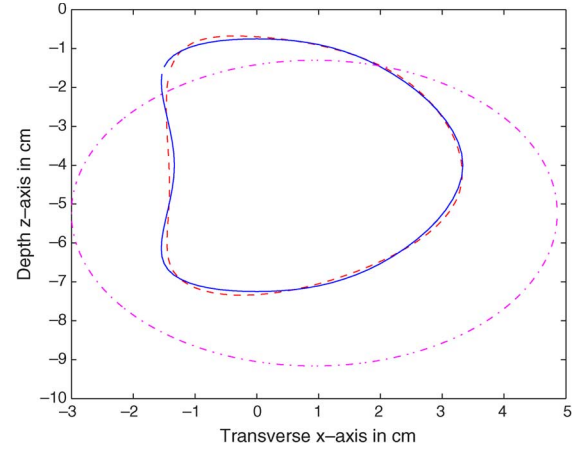


Fig. 6. Phantom S2P1N1 (data SNR = 34.96784 dB) (solid line: actual shape, dotted line: reconstructed shape; dot-dashed line: first estimate). Reconstructed  $f = 0.663515 + i 0.059112$ , and actual  $f = 0.6644 + i 0.0588$ .

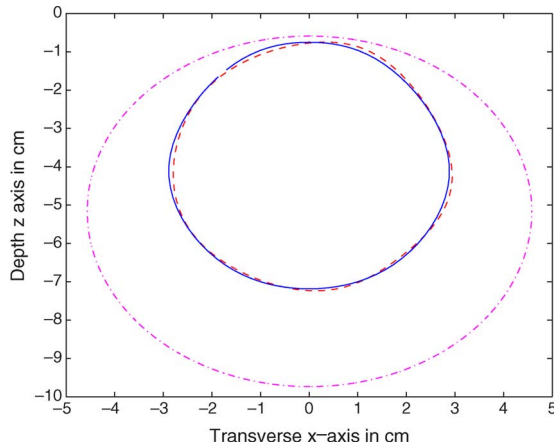


Fig. 4. Phantom S1P2N1 (data SNR = 28.23347 dB) (solid line: actual shape, dotted line: reconstructed shape; dot-dashed line: 1st estimate). Reconstructed  $f = 1.223985 - i 0.029772$ , and actual  $f = 1.2221 - i 0.02667$ .

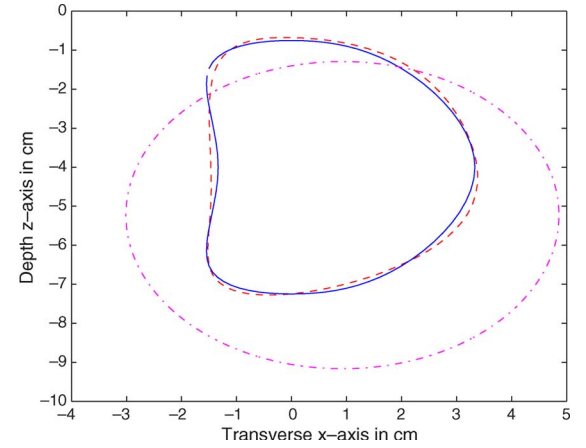


Fig. 7. Phantom S2P1N2 (data SNR = 20.87145 dB) (solid line: actual shape, dotted line: reconstructed shape; dot-dashed line: first estimate). Reconstructed  $f = 0.6520450 + i 0.065861$ , and actual  $f = 0.6644 + i 0.0588$ .

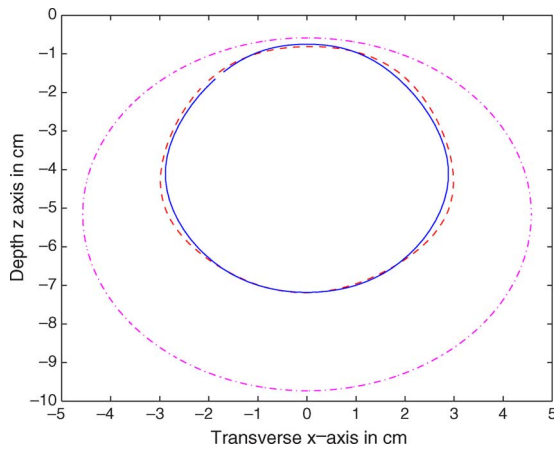


Fig. 5. Phantom S1P2N2 (data SNR = 13.99349 dB) (solid line: actual shape, dotted line: reconstructed shape; dot-dashed line: first estimate). Reconstructed  $f = 1.194527 - i 0.027346$ , and actual  $f = 1.2221 - i 0.02667$ .

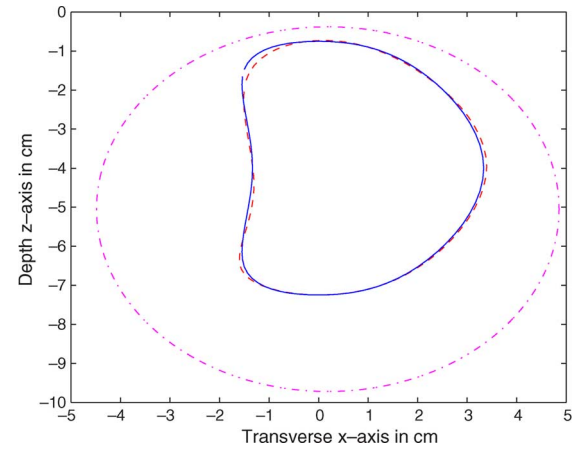


Fig. 8. Phantom S2P2N1 (data SNR = 26.57039 dB) (solid line: actual shape, dotted line: reconstructed shape; dot-dashed line: first estimate). Reconstructed  $f = 1.213768 - i 0.028018$ , and actual  $f = 1.2221 - i 0.02667$ .

we only need to compute the Jacobian inside the object support and, as we observe from Figs. 2–9, the size of the initial support of the object being larger than the actual object (need

not necessarily contain the actual object however), the amount of computation effort for the forward problem reduces as the iterates move toward the actual object.

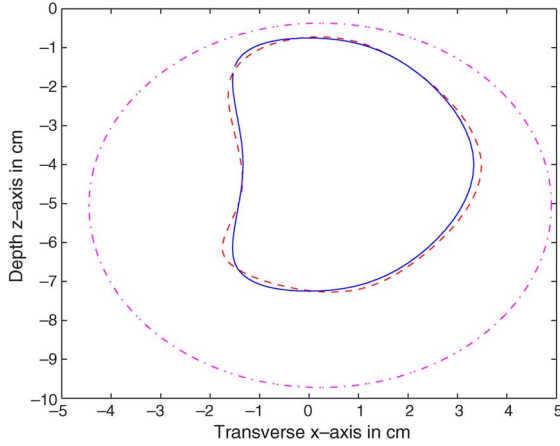


Fig. 9. Phantom S2P2N2 (data SNR = 12.91251 dB) (solid line: actual shape, dotted line: reconstructed shape; dot-dashed line: first estimate). Reconstructed  $f = 1.1819917 - i 0.029987$ , and actual  $f = 1.2221 - i 0.02667$ .

TABLE II  
RECONSTRUCTED VALUES OF  $\text{Re}(f)$  AND  $\text{Im}(f)$

Test case	Reconstructions		Actual	
	$\text{Re}(f)$	$\text{Im}(f)$	$\text{Re}(f)$	$\text{Im}(f)$
P1S1N1	0.66378	0.05474	0.6644	0.0588
P1S1N2	0.656123	0.058301	"	"
P1S2N1	0.663515	0.059112	"	"
P1S2N2	0.6520450	0.065861	"	"
P2S1N1	1.223985	-0.029772	1.2221	-0.02667
P2S1N2	1.194527	-0.027346	"	"
P2S2N1	1.213768	-0.028018	"	"
P2S2N2	1.1819917	-0.029987	"	"

### B. Local Analysis Results

Our objectives of applying the convergence analysis to the preceding results are as an aid in ensuring that the estimate obtained is indeed a part of a convergent sequence and also, at times, to know which iterate to stop at. The spectral radii of the individual components of the convergence matrix are defined as  $\varrho_i = \varrho(\mathbf{K}_i)$ ,  $i = 1, \dots, 4$ , where  $\mathbf{K}_i$  are as defined in (4.14)–(4.17). From those expressions, we observe that, other than the nonlinearities of the problem,  $\varrho_1$ ,  $\varrho_2$ ,  $\varrho_3$ , and  $\varrho_4$  heavily depend on the residual in the data space, the parameter space residual “ $(\mathbf{h} - \mathbf{c})$ ,”  $\mu^2$  and the residual “ $(\mathbf{h} - \mathbf{c})$ ,” and  $1/\mu^2$  and the residual in the objective function space, respectively.

In Tables III and IV, we denote “at termination” as “AT,” “at termination after changing  $\mathbf{c}$  to the value around AT” as “ATc+,” and “ $i$  iterations prior to AT” as “AT-i.”

We see that the values of the data space curvature  $\varrho_1$  are the most important in deciding the choice of a particular estimate as the final correct one. The methodology employed has been to check if the final estimate satisfies the condition  $\varrho(\mathbf{K}) < 1$  as well as  $\varrho_i < 1$  for all  $i$ . If so and also if the iterates have stabilized and/or the relative termination criterion  $\epsilon_{\text{rel}} < 0.01$  is achieved, then the estimates could be considered a part of a convergent sequence. This is reflected in the test cases S1P1N2, S2P1N2, S1P2N1, and S2P2N2.

In cases S1P1N1, S2P1N1, and S2P2N1, the iterates are stable and  $\varrho_1 < 1$ , but  $\varrho_2 > 1$  and  $\varrho(\mathbf{K}) > 1$ . Then, we change

TABLE III  
CONVERGENCE ANALYSIS FOR SHAPE S1

Test case	Iteration	$\mu$	$\varrho_1$	$\varrho_2$	$\varrho_3$	$\varrho_4$	$\varrho(\mathbf{K})$
S1P1N1	AT	0.003125	0.0854	2.1732	0.0661	0.2653	2.0670
	ATc+	0.003125	0.0843	0.2424	0.0072	0.4040	0.4052
S1P1N2	AT	0.025	0.0577	0.0856	0.0792	0.04262	0.1119
S1P2N1	AT	0.0125	0.0658	0.0017	0.0002	0.0490	0.0878
S1P2N2	AT-2	0.05	0.0407	0.8420	0.7316	0.0140	0.86469
	AT-1	0.025	0.0570	1.1140	0.2742	0.04580	1.1393
	AT	0.025	0.0569	1.1145	0.27370	0.0455	1.1395
	ATc+	0.05	0.0495	0.0932	0.0688	0.0108	0.1007
	ATc+c+	0.05	0.0509	0.0311	0.0203	0.0101	0.0429

TABLE IV  
CONVERGENCE ANALYSIS FOR SHAPE S2

Test case	Iteration	$\mu$	$\varrho_1$	$\varrho_2$	$\varrho_3$	$\varrho_4$	$\varrho(\mathbf{K})$
S2P1N1	AT	0.0125	0.0237	1.9535	0.3806	0.0172	1.9659
	ATc+	0.0125	0.0239	0.8815	0.2017	0.0157	0.9026
S2P1N2	AT	0.025	0.0410	0.3443	0.1053	0.03276	0.3599
S2P2N1	AT	0.00625	0.0858	2.0136	0.6031	0.0934	0.0878
	ATc+	0.00625	0.0997	0.0533	0.0204	0.1048	0.1556
S2P2N2	AT	0.0125	0.2993	0.1687	0.0116	0.0014	0.3442

the value of  $\mathbf{c}$  to a more recent iterate and perform another sequence of iterations. Upon applying the analysis to this new sequence, data space curvature  $\varrho_1$  stays comparable to the previous sequence, as do the reconstructed parameters, whereas parameter space curvature  $\varrho_2$  comes down as expected, as does  $\varrho(\mathbf{K})$ , thus justifying the reconstructions.

In case S1P2N2, the analysis is applied to decide which iteration to choose as our estimate since, in this high-noise case, the iterates obtained are not very stable near the termination point. Changing the value of  $\mathbf{c}$  also does not yield a stable sequence; hence, we choose the reconstruction “AT-2” that has the least value of  $\varrho_1$  across the change of  $\mathbf{c}$ . Using our knowledge of the ground truth in the test case, it is also corroborated that the reconstructed parameter values are closer in “AT-2” than in the others.

If  $\mu$  is small enough, then it should be likely that  $\varrho_4 > \varrho_3$ . However, for some problems, as in this paper, it is difficult to reduce  $\mu$  to a very low value, and residual “ $(\mathbf{h} - \mathbf{c})$ ” is also not small enough. This leads to results where  $\varrho_3 > \varrho_4$ . If we want to further reduce  $\mu$ , it is clear that the center “ $\mathbf{c}$ ” must be changed. Of course, if  $\mu$  gets very small, then  $\varrho_4$  will explode. It is thus very possible that the stopping point can be at a point that does not correspond to a “small enough”  $\mu$ .

As we see in the convergence factors, the size of “ $(\mathbf{h} - \mathbf{c})$ ” must not be too large for nonlinear problems, (as well as residual vector “ $\zeta$ ”). In general, if convergence is not achieved, it is possible to investigate the convergence factors, and if the factor with “ $(\mathbf{h} - \mathbf{c})$ ” is too large, one can set “ $\mathbf{c} = \mathbf{h}_k$ ” and continue to iterate. In practice, it is too costly to compute the factors during the iterates, so one can assume that this is the case, which almost often holds (it is problem dependent so one can compute the factors for different cases and learn from it). Note however that, if “ $\mathbf{c}$ ” is changed too often, then the idea of regularization regions is lost, and the method will become a

trust-region method that changes the center in each iteration. Thus, the trust region is about local stabilization (where  $\mathbf{h}_k$  can drift away a lot), and regularization tries to define a region where to find a solution.

## VI. CONCLUSION

A nonlinear Helmholtz-equation-modeled electromagnetic tomographic reconstruction problem is solved for the object boundary and inhomogeneity parameters in a DTRGN solution framework. For an explicit parameterized boundary-representation-based reconstruction scheme, analytical Jacobian calculations are made to express the change in scattered field values w.r.t. changes in the inhomogeneity parameters and the control points in a spline representation of the object boundary, via the use of a level-set representation of the object. Furthermore, analytical expressions have been derived for the Hessian matrix, and the reconstructed estimates obtained by the DTRGN method have been analyzed for convergence by the application of a local Hessian-based convergence analysis to the scheme. Numerical results demonstrating the present reconstruction scheme and its analysis are presented for a subsurface imaging problem for small minelike dielectric objects. We note that, in addition to the shape and the real part of the electrical parameter  $\alpha$ , good agreement has also been observed in the reconstructions of  $\text{Im}(\alpha)$ . We also indicate some real-world issues that are addressable in the framework of this paper and are the focus of forthcoming work.

- 1) The problem of reconstructing 3-D objects in a nonhomogeneous (typically layered) background [36], [37] is an important computationally demanding one. The ability to find objects in a nonhomogeneous background is implicit in this paper's formulation, in that one needs to compute the incident fields for that background and express the unknown in basis containing more terms than just the constant term in the general representation (2.11). As mentioned in Section III, the extension of the preceding method to three dimensions would involve the choice of suitable basis representations for the shapes, as well as defining a tube in 3-D as consisting of all parallel surfaces  $\Upsilon^\lambda(x, y, z) = \Upsilon(x, y, z) + \lambda \hat{n}(x, y, z)$  such that  $|\lambda| < 1/C$ , where  $\hat{n}(x, y, z)$  is the standard unit normal and  $C$  is a positive constant greater than the absolute values of both the principal curvatures of the surface.
- 2) In this paper, we have fixed the number of reconstructed control points since we analyzed reconstructions for different shapes, noise levels, and material compositions, with an emphasis on the almost-rank-deficient nature of the inverse problem. As mentioned in Section II, a realistic problem would have to solve a series of "surrogate" subinverse-problems, from lesser number of control points to larger numbers; each problem however has to be separately regularized due to its possible ill-posed rank-deficient nature.
- 3) The amount of data needed to generate acceptable reconstructions needs to be studied since one rationale of reducing the number of unknowns is to use less data than usual. Equally, in the light of the physical assumptions

made, the amount of data that would at all be used by the reconstruction algorithm needs to be understood.

- 4) If we have *a priori* information about the number of objects, then, (using level-set-based representations for multiple regions such as those mentioned in [13]), that information could be incorporated into the present framework (after suitable initialization of the nonlinear iterations) by augmenting the unknown vectors for each region. If we do not have such *a priori* information, then, it seems that suitable thresholding (i.e., lower limits on the size of the tubular neighborhood coupled with mutual distances of control points) and reinitialization schemes need to be investigated to address the merging or splitting of regions.

## APPENDIX A

*Lemma:* Defining  $H_\rho(\cdot)$  by (2.9) and denoting the level-set function at a point  $(x, y)$  by  $\phi(x, y)$ , we have the result

$$\lim_{\rho \rightarrow 0} H'_\rho[\phi(x, y)] = \frac{\delta[\phi(x, y)]}{|\nabla\phi(x, y)|}. \quad (\text{A1})$$

*Proof:* Parameterizing the curve  $\phi(x, y) = 0$  as  $x = s_1(\tau)$ ,  $y = s_2(\tau)$ , we have on  $\Gamma(\equiv \{\phi(s_1(\tau), s_2(\tau)) = 0\})$

$$\phi_x \dot{s}_1(\tau) + \phi_y \dot{s}_2(\tau) = 0.$$

Choosing  $(s_1, s_2)$ , so that  $\Gamma$  is a unit speed curve, we set

$$\dot{s}_1 = \frac{\phi_x}{\phi_x^2 + \phi_y^2}, \quad \dot{s}_2 = -\frac{\phi_y}{\phi_x^2 + \phi_y^2}.$$

The unit normal vector is given by

$$(n_1(\tau), n_2(\tau)) = \frac{(\phi_x, \phi_y)}{\sqrt{\phi_x^2 + \phi_y^2}}.$$

Thus, for  $\gamma \in [-\rho, \rho]$ ,  $\tau \in [0, L]$ , where  $L$  is the total arc length, a strip around  $\Gamma$ , which is denoted by  $\Gamma_\rho$  and constructed as

$$\begin{aligned} \Gamma_\rho &\equiv \{(x(\gamma, \tau), y(\gamma, \tau))\} \\ &= \{(s_1(\tau) + \gamma n_1(\tau), s_2(\tau) + \gamma n_2(\tau))\} \end{aligned}$$

is unique and smooth from  $[-\rho, \rho] \times [0, L]$  into  $\Gamma_\rho$ .

Now, from (2.9), we can write

$$H'_\rho[\phi(\mathbf{r})] := \begin{cases} \frac{1}{2\rho} \left\{ 1 + \cos\left(\frac{\pi\phi(\mathbf{r})}{\rho}\right) \right\}, & \text{if } \mathbf{r} \in \phi^{-1}[-\rho, \rho] \\ 0, & \text{otherwise.} \end{cases} \quad (\text{A2})$$

Thus,  $\text{Supp}(H'_\rho[\phi(x, y)]) \subset \Gamma_\rho$ . Defining  $C_\rho(\mathbf{r}) \equiv \{1 + \cos((\pi\phi(\mathbf{r})/\rho))\}$ , for  $v \in C(\bar{\Omega})$ , we have

$$\begin{aligned} \lim_{\rho \rightarrow 0} \int_{\Gamma_\rho} H'_\rho[\phi(x, y)] v(x, y) dx dy \\ = \lim_{\rho \rightarrow 0} \int_{[-\rho, \rho] \times [0, L]} \frac{C_\rho(\gamma, \tau)}{2\rho} v(\gamma, \tau) \left| \frac{\partial(x, y)}{\partial(\gamma, \tau)} \right| d\gamma d\tau \quad (\text{A3}) \end{aligned}$$

where

$$\begin{aligned} \frac{\partial(x, y)}{\partial(\gamma, \tau)} &= n_1(\dot{s}_2 + \gamma\dot{n}_2) - n_2(\dot{s}_1 + \gamma\dot{n}_1) \\ &= \frac{1}{\sqrt{\phi_x^2 + \phi_y^2}} + \gamma(n_1\dot{n}_2 - n_2\dot{n}_1). \end{aligned} \quad (\text{A4})$$

Recalling the fact that, for a smooth-enough function  $P(\gamma)$  and small-enough  $\rho$

$$\begin{aligned} \frac{1}{2\rho} \int_{-\rho}^{\rho} P(\gamma) C_{\rho}(\gamma, \tau) d\gamma \\ = \frac{P(0)}{2\rho} \int_{-\rho}^{\rho} C_{\rho}(\gamma, \tau) d\gamma + \frac{P'(0)}{2\rho} \int_{-\rho}^{\rho} \gamma C_{\rho}(\gamma, \tau) d\gamma \end{aligned} \quad (\text{A5})$$

and since close enough to the boundary,  $\phi(\gamma, \tau) \simeq \gamma$ , we have

$$\begin{aligned} \lim_{\rho \downarrow 0} \frac{1}{2\rho} \int_{-\rho}^{\rho} P(\gamma) C_{\rho}(\gamma, \tau) d\gamma &= \lim_{\rho \downarrow 0} \frac{P(0)}{2\rho} \int_{-\rho}^{\rho} \left( 1 + \cos\left(\frac{\pi\gamma}{\rho}\right) \right) d\gamma \\ &\quad + \lim_{\rho \downarrow 0} \frac{P'(0)}{2\rho} \int_{-\rho}^{\rho} \gamma C_{\rho}(\gamma, \tau) d\gamma \\ &= P(0). \end{aligned} \quad (\text{A6})$$

Using (A4), (A6), and the observation that the second term in the right-hand side of (A4) has only  $\gamma$  as the  $\gamma$ -dependent term, in (A3), we have

$$\begin{aligned} \lim_{\rho \downarrow 0} \int_{\Gamma_{\rho}} H'_{\rho}[\phi(x, y)] v(x, y) dx dy \\ = \int_0^L d\tau \lim_{\rho \downarrow 0} \frac{1}{2\rho} \int_{-\rho}^{\rho} C_{\rho}(\gamma, \tau) \frac{v(x(\gamma, \tau), y(\gamma, \tau))}{\sqrt{\phi_x^2 + \phi_y^2}} d\gamma \\ = \int_0^L \frac{v(s_1(\tau), s_2(\tau))}{\sqrt{\phi_x^2 + \phi_y^2}} d\tau. \end{aligned} \quad (\text{A7})$$

Hence, we have the proof.  $\blacksquare$

## APPENDIX B

### Jacobian and Hessian Evaluations

*Jacobian Calculations:* For the B-spline representation of the boundary curve, the Jacobian entries can be explicitly written as follows:

$$\frac{\partial\vartheta_i}{\partial x_q} = - \sum_{j \ni (\mathbf{r}_j \in \phi^{-1}[-\rho, \rho])} \tilde{N}_{q,k}(s_j) \frac{\partial\vartheta_i}{\partial f_j} \alpha H'_{\rho}[\phi(\mathbf{r}_j)] \phi_x(s_j) \quad (\text{B1})$$

where  $\phi_x(\cdot)$  denotes the partial derivative of  $\phi(\cdot)$  with respect to the  $x$ -coordinate. Furthermore

$$\frac{\partial\vartheta_i}{\partial z_q} = - \sum_{j \ni (\mathbf{r}_j \in \phi^{-1}[-\rho, \rho])} \tilde{N}_{q,k}(s_j) \frac{\partial\vartheta_i}{\partial f_j} \alpha H'_{\rho}[\phi(\mathbf{r}_j)] \phi_z(s_j) \quad (\text{B2})$$

$$\frac{\partial\vartheta_i}{\partial \alpha} = \sum_j \frac{\partial\vartheta_i}{\partial f_j} H_{\rho}[\phi(\mathbf{r}_j)]. \quad (\text{B3})$$

*Hessian Evaluation:* In order to calculate the boundary variations  $\delta\varphi$ , where  $\varphi = \phi_x, \phi_z$ , we use the following relation:

$$(\varphi + \delta\varphi)[(\Upsilon + \delta\Upsilon)(s)] = \delta\varphi[\Upsilon(s)] + \nabla\varphi \cdot \delta\Upsilon(s) \quad (\text{B4})$$

where we recall from (3.15)

$$\delta\Upsilon(s) = \sum_{q=1}^{M_p} \tilde{N}_{q,k}(s) \delta\Upsilon_q^c.$$

Defining, for a given  $s$ ,  $P(\Upsilon^c) \equiv \varphi[\Upsilon(s)]$ , we have

$$P(\Upsilon^c + \delta\Upsilon^c) = (\varphi + \delta\varphi)[(\Upsilon + \delta\Upsilon)(s)].$$

Hence, up to first order, we can write

$$P(\Upsilon^c + \delta\Upsilon^c) = (\varphi + \delta\varphi)[(\Upsilon + \delta\Upsilon)(s)]$$

where  $\mathbf{J}_P$  is the Jacobian of  $P(\cdot)$  w.r.t.  $\Upsilon^c$ . Hence, we can write up to first order

$$(\varphi + \delta\varphi)[(\Upsilon + \delta\Upsilon)(s)] - \varphi[\Upsilon(s)] = \mathbf{J}_P \delta\Upsilon^c.$$

Hence, we have from (B4)

$$\delta\varphi[\Upsilon(s)] = \mathbf{J}_P \delta\Upsilon^c - \nabla\varphi \cdot \left( \sum_{q=1}^{M_p} \tilde{N}_{q,k}(s) \delta\Upsilon_q^c \right) \quad (\text{B5})$$

where  $\mathbf{J}_P$  can be numerically evaluated via finite differences. However, note that, although finite differences are employed in the preceding calculation, no new forward problem evaluations are involved here.

To evaluate the Hessian, we observe the following relations:

$$\frac{\partial f_j}{\partial x_q} = -\tilde{N}_{q,k}(s_j) \alpha H'_{\rho}[\phi(\mathbf{r}_j)] \phi_x(s_j)$$

$$\frac{\partial f_j}{\partial z_q} = -\tilde{N}_{q,k}(s_j) \alpha H'_{\rho}[\phi(\mathbf{r}_j)] \phi_z(s_j)$$

$$\frac{\partial f_j}{\partial \alpha} = H_{\rho}[\phi(\mathbf{r}_j)].$$

Thus, the Hessian relations can be written as

$$\frac{\partial^2 \vartheta_i}{\partial x_p \partial x_q} = \mathcal{T}_{xx}^{(1)} + \mathcal{T}_{xx}^{(2)} + \mathcal{T}_{xx}^{(3)} \quad (\text{B6})$$

where

$$\mathcal{T}_{xx}^{(1)} = -\sum_j \tilde{N}_{q,k}(s_j) \left\{ \sum_l \frac{\partial^2 \vartheta_i}{\partial f_l \partial f_j} \frac{\partial f_l}{\partial x_p} \right\} \alpha H'_\rho [\phi(\mathbf{r}_j)] \phi_x(s_j)$$

where the expression for  $\frac{\partial^2 \vartheta_i}{\partial f_l \partial f_j}$  in the method-of-moments framework is given in Appendix C.

$$\begin{aligned} \mathcal{T}_{xx}^{(2)} &= \sum_j \left\{ -\tilde{N}_{q,k}(s_j) \phi_x(s_j) \right\} \frac{\partial \vartheta_i}{\partial f_j} \\ &\quad \times \alpha H''_\rho [\phi(\mathbf{r}_j)] \left\{ -\tilde{N}_{p,k}(s_j) \phi_x(s_j) \right\} \\ \mathcal{T}_{xx}^{(3)} &= -\sum_j \tilde{N}_{q,k}(s_j) \frac{\partial \vartheta_i}{\partial f_j} \alpha H'_\rho [\phi(\mathbf{r}_j)] \\ &\quad \times \left\{ J_P(x_p) - \phi_{xx} \tilde{N}_{p,k}(s_j) \right\} \end{aligned}$$

where  $J_P(x_p)$  denotes the term of  $\mathbf{J}_P$  corresponding to control point  $x_p$ . Note that the summation indexes  $j$  and  $l$  will be such that  $\mathbf{r}_j \in \phi^{-1}[-\rho, \rho]$  and  $\mathbf{r}_l \in \phi^{-1}[-\rho, \rho]$  whenever there are  $H'_\rho[\cdot]$  or  $H''_\rho[\cdot]$  in any product term component of the summation. Furthermore

$$\frac{\partial^2 \vartheta_i}{\partial z_p \partial z_q} = \mathcal{T}_{zz}^{(1)} + \mathcal{T}_{zz}^{(2)} + \mathcal{T}_{zz}^{(3)} \quad (\text{B7})$$

where

$$\begin{aligned} \mathcal{T}_{zz}^{(1)} &= -\sum_j \tilde{N}_{q,k}(s_j) \left\{ \sum_l \frac{\partial^2 \vartheta_i}{\partial f_l \partial f_j} \frac{\partial f_l}{\partial z_p} \right\} \alpha H'_\rho [\phi(\mathbf{r}_j)] \phi_z(s_j) \\ \mathcal{T}_{zz}^{(2)} &= \sum_j \left\{ -\tilde{N}_{q,k}(s_j) \phi_z(s_j) \right\} \frac{\partial \vartheta_i}{\partial f_j} \\ &\quad \times \alpha H''_\rho [\phi(\mathbf{r}_j)] \left\{ -\tilde{N}_{p,k}(s_j) \phi_z(s_j) \right\} \\ \mathcal{T}_{zz}^{(3)} &= -\sum_j \tilde{N}_{q,k}(s_j) \frac{\partial \vartheta_i}{\partial f_j} \alpha H'_\rho [\phi(\mathbf{r}_j)] \\ &\quad \times \left\{ J_P(z_p) - \phi_{zz} \tilde{N}_{p,k}(s_j) \right\}. \end{aligned}$$

In addition,

$$\frac{\partial^2 \vartheta_i}{\partial \alpha^2} = \sum_j \left\{ \sum_l \frac{\partial^2 \vartheta_i}{\partial f_l \partial f_j} \frac{\partial f_l}{\partial \alpha} \right\} H_\rho [\phi(\mathbf{r}_j)]. \quad (\text{B8})$$

The mixed derivatives are

$$\frac{\partial^2 \vartheta_i}{\partial z_p \partial x_q} = \mathcal{T}_{xz}^{(1)} + \mathcal{T}_{xz}^{(2)} + \mathcal{T}_{xz}^{(3)} \quad (\text{B9})$$

where

$$\begin{aligned} \mathcal{T}_{xz}^{(1)} &= -\sum_j \tilde{N}_{q,k}(s_j) \left\{ \sum_l \frac{\partial^2 \vartheta_i}{\partial f_l \partial f_j} \frac{\partial f_l}{\partial z_p} \right\} \\ &\quad \times \alpha H'_\rho [\phi(\mathbf{r}_j)] \phi_x(s_j) \\ \mathcal{T}_{xz}^{(2)} &= \sum_j \left\{ -\tilde{N}_{q,k}(s_j) \phi_x(s_j) \right\} \frac{\partial \vartheta_i}{\partial f_j} \\ &\quad \times \alpha H''_\rho [\phi(\mathbf{r}_j)] \left\{ -\tilde{N}_{p,k}(s_j) \phi_z(s_j) \right\} \\ \mathcal{T}_{xz}^{(3)} &= -\sum_j \tilde{N}_{q,k}(s_j) \frac{\partial \vartheta_i}{\partial f_j} \alpha H'_\rho [\phi(\mathbf{r}_j)] \\ &\quad \times \left\{ J_P(z_p) - \phi_{xz} \tilde{N}_{p,k}(s_j) \right\}. \end{aligned}$$

In addition

$$\frac{\partial^2 \vartheta_i}{\partial x_q \partial \alpha} = \mathcal{T}_{x\alpha}^{(1)} + \mathcal{T}_{x\alpha}^{(2)} \quad (\text{B10})$$

where

$$\begin{aligned} \mathcal{T}_{x\alpha}^{(1)} &= -\sum_j \tilde{N}_{q,k}(s_j) \left\{ \sum_l \frac{\partial^2 \vartheta_i}{\partial f_l \partial f_j} H_\rho [\phi(\mathbf{r}_l)] \right\} \\ &\quad \times \alpha H'_\rho [\phi(\mathbf{r}_j)] \phi_x(s_j) \\ \mathcal{T}_{x\alpha}^{(2)} &= \sum_j \left\{ -\tilde{N}_{q,k}(s_j) \phi_x(s_j) \right\} \frac{\partial \vartheta_i}{\partial f_j} H'_\rho [\phi(\mathbf{r}_j)]. \end{aligned}$$

## APPENDIX C

### Method-of-Moments-Based Jacobian and Hessian

From Section III-B, we recall the basis decompositions (3.11) of the following forms for parameter function  $f(\cdot)$  and field  $u(\cdot)$ :

$$f(\mathbf{r}) = \sum_{j=1}^n f_j \psi_j(\mathbf{r}) \quad u(\mathbf{r}, \omega) = \sum_{j=1}^n u_j(\omega) \psi_j(\mathbf{r})$$

where  $n$  is the number of pixels in the image, and  $\{\psi_j(\mathbf{r})\}$  is an appropriate basis set; in our case, we choose it to be the pulse basis, i.e.,  $\psi_j(\mathbf{r}) = 1$  for  $\mathbf{r} \in \text{pixel } j$  and zero otherwise.

Substituting (3.11) in (2.6), we get

$$u_{\text{sc}}(\mathbf{r}, \omega) = \sum_{j=1}^n f_j u_j(\mathbf{f}, \omega) o_j(\mathbf{r}, \omega) \quad (\text{C1})$$

where

$$o_j(\mathbf{r}, \omega) = \int_{\Omega} g(\mathbf{r}, \mathbf{r}', \omega) k_{\text{amb}}^2(\mathbf{r}', \omega) \psi_j(\mathbf{r}') d\mathbf{r}'. \quad (\text{C2})$$

Considering a point-matching scheme [25], we obtain the expression for the field at a point  $\mathbf{r} = \mathbf{r}_i$ , from (C1) and (2.4), as

$$u(\mathbf{r}_i, \omega) = u_{\text{amb}}(\mathbf{r}_i, \omega) + \sum_{j=1}^n f_j u_j(\mathbf{f}, \omega) o_j(\mathbf{r}_i, \omega).$$



Define matrices  $\mathbf{G}_R$  and  $\mathbf{G}_D$  corresponding to the sets of receiver points (denoted by  $\mathcal{R}$ ) and object-domain points (denoted by  $\mathcal{D}$ ), respectively, as follows:

$$\begin{aligned} G_R(i, j) &= o_j(\mathbf{r}_i, \omega) \quad \text{for } \mathbf{r}_i \in \mathcal{R} \\ G_D(i, j) &= o_j(\mathbf{r}_i, \omega) \quad \text{for } \mathbf{r}_i \in \mathcal{D} \end{aligned}$$

where  $o_j(\mathbf{r}, \omega)$  has been defined in (C2), and the  $\omega$  dependence in the matrices on the left-hand side have been suppressed for ease of notation.

The Jacobian matrix  $\mathbf{J}(\mathbf{f})$  is obtained as

$$\mathbf{J} = [\mathbf{J}_{\mathbf{q},s}]$$

where  $[\mathbf{J}_{\mathbf{q},s}]$  is the stacked version of the matrices  $\mathbf{J}_{\mathbf{q},n}$  for each source frequency  $\omega_q$  and source position  $s$ , with  $\mathbf{J}_{\mathbf{q},s}$  being given by [35]

$$\mathbf{J}_{\mathbf{q},s} = -\mathbf{G}_R(\mathbf{I} - \Lambda \mathbf{G}_D)^{-1} \text{diag}(\mathbf{u}_{q,s}^{\text{int}}).$$

Using the following relation [1]:

$$(\mathbf{I} - \Lambda \mathbf{G}_D)^{-1} = \mathbf{I} + \Lambda(\mathbf{I} - \mathbf{G}_D \Lambda)^{-1} \mathbf{G}_D$$

we obtain a column of the Jacobian matrix as

$$\frac{\partial \vartheta}{\partial f_i} = -(G_R(:, i) + \mathbf{G}_R \Lambda \mathbf{C}^{-1} G_D(:, i)) u_i(\mathbf{f}) \quad (\text{C3})$$

where  $(:, i)$  in the argument of a matrix denotes the  $i$ th column of the matrix (in Matlab notation). Hence, a second-derivative column vector can be written as

$$\begin{aligned} \frac{\partial^2 \vartheta}{\partial f_i \partial f_j} &= -(G_R(:, i) + \mathbf{G}_R \Lambda \mathbf{C}^{-1} G_D(:, i)) \frac{\partial u_i(\mathbf{f})}{\partial f_j} \\ &\quad - \left( \mathbf{G}_R^j \mathbf{C}^{-1} + \mathbf{G}_R \Lambda \left( \mathbf{C}^{-1} \mathbf{G}_D^j \mathbf{C}^{-1} \right) \right) G_D(:, i) u_i(\mathbf{f}) \quad (\text{C4}) \end{aligned}$$

where  $\mathbf{G}_R^j$  ( $\mathbf{G}_D^j$ ) is the matrix obtained by the zeroing out all columns of  $\mathbf{G}_R$  ( $\mathbf{G}_D$ ), except the  $j$ th column.

#### ACKNOWLEDGMENT

The authors would like to thank the anonymous reviewers for their comments, which have helped improve the presentation of this paper. N. Naik would like to thank Dr. S. Mahajan of IIT, Mumbai, India, and Dr. V. Rao for some very useful discussions and Dr. G. Spanos of NRL, Washington, DC, for the very useful pointers.

#### REFERENCES

- [1] R. F. Remis and P. M. van den Berg, "On the equivalence of the Newton–Kantorovich and distorted Born methods," *Inv. Prob.*, vol. 16, no. 1, pp. L1–L4, Feb. 2000.
- [2] N. Naik, J. Eriksson, and H. Sahli, "An analysis of a Tikhonov regularized Gauss–Newton reconstruction approach to GPR tomography," in *Proc. 10th Int. Conf. Ground Penetrating Radar*, Delft, The Netherlands, Jun. 21–24, 2004, pp. 67–70.
- [3] A. Abubakar, T. M. Habashy, V. L. Druskin, and L. Knizhnerman, "An enhanced Gauss–Newton inversion algorithm using a dual-optimal grid approach," *IEEE Trans. Geosci. Remote Sens.*, vol. 44, no. 6, pp. 1419–1427, Jun. 2006.
- [4] P. M. van den Berg and A. Abubakar, "Linear and nonlinear inversion of GPR data," in *Proc. 2nd Int. Workshop Advanced GPR*, Delft, The Netherlands, May 14–16, 2003, pp. 156–163.
- [5] C. Estatico, M. Pastorino, and A. Randazzo, "An inexact-Newton method for short-range microwave imaging within the second-order Born approximation," *IEEE Trans. Geosci. Remote Sens.*, vol. 43, no. 11, pp. 2593–2605, Nov. 2005.
- [6] T. Cui, Y. Qin, Y. Ye, J. Wu, G. L. Wang, and W. C. Chew, "Efficient low-frequency inversion of 3-D buried objects with large contrasts," *IEEE Trans. Geosci. Remote Sens.*, vol. 44, no. 1, pp. 3–9, Jan. 2006.
- [7] E. L. Miller, M. Kilmer, and C. Rappaport, "A new shape based object localization and characterization from scattered field data," *IEEE Trans. Geosci. Remote Sens.*, vol. 38, no. 4, pp. 1682–1696, Jul. 2000.
- [8] S. Bonnard, M. Saillard, and P. Vincent, "Improved inverse scattering for dielectric homogeneous cylinders," *J. Opt. A, Pure Appl. Opt.*, vol. 4, no. 1, pp. 566–572, 1999.
- [9] M. E. Kilmer, E. L. Miller, A. Barbaro, and D. Boas, "Three dimensional shape-based imaging of absorption perturbation for diffuse optical tomography," *Appl. Opt.*, vol. 42, no. 16, pp. 3129–3144, Jun. 1, 2003.
- [10] J. C. Ye, Y. Bresler, and P. Moulin, "Cramer–Rao bounds for 2-D target shape estimation in nonlinear inverse scattering problems with application to passive radar," *IEEE Trans. Antennas Propag.*, vol. 49, no. 5, pp. 771–783, May 2001.
- [11] O. Dorn, E. L. Miller, and C. M. Rappaport, "A shape reconstruction method for electromagnetic tomography using adjoint fields and level sets," *Inv. Prob.*, vol. 16, no. 5, pp. 1119–1156, Oct. 2000.
- [12] H. Feng, W. C. Karl, and D. A. Castanon, "A curve evolution approach to object-based tomographic reconstruction," *IEEE Trans. Image Process.*, vol. 12, no. 1, pp. 44–57, Jan. 2003.
- [13] E. T. Chung, T. F. Chan, and X. C. Tai, "Electrical impedance tomography using level set representation and total variational regularization," *J. Comput. Phys.*, vol. 205, no. 1, pp. 357–372, May 2005.
- [14] J. Eriksson, "Optimization and regularization of nonlinear least squares problems," Ph.D. dissertation, Dept. Comput. Sci., Umeå Univ., Umeå, Sweden, 1996.
- [15] A. D. Zacharopoulos, S. R. Arridge, O. Dorn, V. Kolehmainen, and J. Sikora, "Three-dimensional reconstruction of shape and piecewise constant region values for optical tomography using spherical harmonic parameterization and a boundary element method," *Inv. Prob.*, vol. 22, no. 5, pp. 1509–1532, Oct. 2006.
- [16] R. Firoozabadi, E. L. Miller, C. M. Rappaport, and A. W. Morgenthaler, "Subsurface sensing of buried objects under a randomly rough surface using scattered electromagnetic field data," *IEEE Trans. Geosci. Remote Sens.*, vol. 45, no. 1, pp. 104–117, Jan. 2007.
- [17] O. Dorn and D. Lesselier, "Level set methods for inverse scattering," *Inv. Prob.*, vol. 22, no. 4, pp. R67–R131, Aug. 2006.
- [18] F. Santosa, "A level set approach for inverse problems involving obstacles," *ESAIM: Control, Optim. Calc. Var.*, vol. 1, pp. 17–33, 1996.
- [19] Y. A. Gryazin, M. V. Klibanov, and T. R. Lucas, "Two numerical methods for an inverse problem for the 2-D Helmholtz equation," *J. Comput. Phys.*, vol. 184, no. 1, pp. 122–148, Jan. 2003.
- [20] M. Cheney and D. Isaacson, "Inverse problems for a perturbed dissipative half-space," *Inv. Prob.*, vol. 11, no. 4, pp. 865–868, 1995.
- [21] N. Naik and H. Sahli, "The forward problem for two-dimensional Helmholtz equation modelled GPR tomography based upon the method of moments," Vrije Universiteit Brussels, Brussels, Belgium, ETRO-IRIS Tech. Rep. TR–089, Nov. 2003.
- [22] W. C. Chew, G. P. Otto, W. H. Weedon, J. H. Lin, C. C. Lu, Y. M. Wang, and M. Moghaddam, "Nonlinear diffraction tomography—The use of inverse scattering for imaging," *Int. J. Imaging Sys. Technol.*, vol. 7, pp. 16–24, Jan. 1996.
- [23] T. F. Chan and L. Vese, "Active contours without edges," *IEEE Trans. Image Process.*, vol. 10, no. 2, pp. 266–277, Feb. 2001.
- [24] A. Blake and M. Isard, *Active Contours*. London, U.K.: Springer-Verlag, 1998.
- [25] S. M. Rao and G. K. Gothard, "Integral equations," in *Wiley Encyclopedia of Electrical and Electronics Engineering*, J. Webster, Ed. Hoboken, NJ: Wiley, pp. 351–361.
- [26] G. E. Bredon, *Topology and Geometry*. New York: Springer-Verlag, 1997.
- [27] R. Kress, *Linear Integral Equations*. New York: Springer-Verlag, 1999.
- [28] A. Presley, *Elementary Differential Geometry*. New York: Springer-Verlag, 2001.
- [29] J. Nocedal and J. Wright, *Numerical Optimization*, ser. Springer Series in Operations Research. New York: Springer-Verlag, 1999.



- [30] B. Kaltenbacher, "Some Newton-type methods for the regularization of nonlinear ill-posed problems," *Inv. Prob.*, vol. 13, no. 3, pp. 729–753, Jun. 1997.
- [31] R. Ramlau, "TIGRA—An iterative algorithm for regularizing nonlinear ill-posed problems," *Inv. Prob.*, vol. 19, no. 2, pp. 433–465, Apr. 2003.
- [32] A. W. Bakushinskii, "The problem of the convergence of the iteratively regularized Gauss–Newton method," *Comput. Math. Math. Phys.*, vol. 32, no. 9, pp. 1353–1359, Sep. 1992.
- [33] T. M. Habashy and A. Abubakar, "A general framework for constraint minimization for the inversion of electromagnetic measurements," *Progr. Electromagn. Res.*, vol. 46, pp. 265–312, 2004.
- [34] H. Ramsin and P.-A. Wedin, "A comparison of some algorithms for the nonlinear least squares problem," *BIT Numer. Math.*, vol. 17, no. 1, pp. 72–90, Mar. 1977.
- [35] N. Joachimowitz, C. Pichot, and P. Hugonin, "Inverse scattering: An iterative numerical method for electromagnetic scattering," *IEEE Trans. Antennas Propag.*, vol. AP-39, no. 12, pp. 1742–1752, Dec. 1991.
- [36] F. Li, Q. H. Liu, and L.-P. Song, "Three-dimensional reconstruction of objects buried in layered media using Born and distorted Born iterative methods," *IEEE Geosci. Remote Sens. Lett.*, vol. 1, no. 2, pp. 107–111, Apr. 2004.
- [37] L.-P. Song and Q. H. Liu, "Fast three-dimensional electromagnetic nonlinear inversion in layered media with a novel scattering approximation," *Inv. Prob.*, vol. 20, no. 6, pp. S171–S194, Dec. 2004.



**Naren Naik** was born in Bangalore, India, in 1970. He received the B.Sc. degree in physics, mathematics, and electronics from Bangalore University, Bangalore, in 1988 and the M.E. degree in electrical communication engineering and the Ph.D. degree for his work on studies on the development of models and reconstruction algorithms in optical tomography from the Indian Institute of Science (IISc), Bangalore, in 1992 and 2000, respectively.

From 2001 to 2004, he was a Postdoctoral Research Associate with ETRO-IRIS, Vrije Universiteit Brussel, Brussels, Belgium, where he worked on the Concerted Research Action (GOA) Project "Numerical issues in tomographic shallow subsurface imaging." From 2005 to 2006, he was with the Optical Tomography Laboratory, IISc. He is currently with the Department of Mechanical Engineering, College of Engineering, University of Canterbury, Christchurch, New Zealand. His current research interests are the development and analysis of reconstruction approaches to tomographic imaging, nonlinear inverse problems, and scattering theory.



radio network systems.

**Jerry Eriksson** was born in Luleå, Sweden, in June 1963. He received the B.S. degree in mathematics, the M.S. degree in computing science, and the Ph.D. degree in numerical optimization and regularization from Umeå University, Umeå, Sweden, in 1987, 1990, and 1996, respectively.

During 1997–2000, he was with Ericsson Telecom company, where he worked on telesystems. He is currently with the Department of Computing Science, Umeå University. His current research interests include the optimization of inverse problems and



**Pieter de Groen** was born in The Netherlands in 1944. He received the Ph.D. degree in mathematics from the Free University of Amsterdam, Amsterdam, The Netherlands, in 1976.

He is currently with the Department of Mathematics, Vrije Universiteit Brussel, Brussels, Belgium, teaching numerical analysis. His research interests are singular perturbations and numerical approximations of differential equations.



**Hichem Sahli** received the Ph.D. degree in computer sciences from the Ecole Nationale Supérieure de Physique de Strasbourg, Strasbourg, France, in 1991, and the "Habilitation à diriger des recherches" in 1996.

Since 1999, he has been a Professor with the Department of Electronics and Informatics (ETRO), Vrije Universiteit Brussel, Brussels, Belgium, and Group-Coordinator with the Interuniversitair Micro-Elektronica Centrum, Leuven, Belgium. He coordinates the research team in computer vision within ETRO. His principal research fields are inverse problems in computer vision and image analysis.